



ELSEVIER

Contents lists available at SciVerse ScienceDirect

Journal of the Mechanics and Physics of Solids

journal homepage: www.elsevier.com/locate/jmps

Slip transfer and plastic strain accumulation across grain boundaries in Hastelloy X

Wael Z. Abuzaid^a, Michael D. Sangid^b, Jay D. Carroll^a, Huseyin Sehitoglu^{a,*}, John Lambros^c

^a Department of Mechanical Science and Engineering, University of Illinois at Urbana-Champaign, 1206W. Green St., Urbana, IL 61801, USA

^b School of Aeronautics and Astronautics, Purdue University, 701W. Stadium Ave., West Lafayette, IN 47907, USA

^c Department of Aerospace Engineering, University of Illinois at Urbana-Champaign, 104S. Wright St., Urbana, IL 61801, USA

ARTICLE INFO

Article history:

Received 18 August 2011

Received in revised form

1 February 2012

Accepted 2 February 2012

Keywords:

Grain boundaries

Microstructures

Dislocations

Polycrystalline material

Slip transmission

ABSTRACT

In this study, high resolution *ex situ* digital image correlation (DIC) was used to measure plastic strain accumulation with sub-grain level spatial resolution in uniaxial tension of a nickel-based superalloy, Hastelloy X. In addition, the underlying microstructure was characterized with similar spatial resolution using electron backscatter diffraction (EBSD). With this combination of crystallographic orientation data and plastic strain measurements, the resolved shear strains on individual slip systems were spatially calculated across a substantial region of interest, *i.e.*, we determined the local slip system activity in an aggregate of ~ 600 grains and annealing twins. The full-field DIC measurements show a high level of heterogeneity in the plastic response with large variations in strain magnitudes within grains and across grain boundaries (GBs). We used the experimental results to study these variations in strain, focusing in particular on the role of slip transmission across GBs in the development of strain heterogeneities. For every GB in the polycrystalline aggregate, we have established the most likely dislocation reaction and used that information to calculate the residual Burgers vector and plastic strain magnitudes due to slip transmission across each interface. We have also used molecular dynamics simulations (MD) to establish the energy barriers to slip transmission for selected cases yielding different magnitudes of the residual Burgers vector. From our analysis, we show an inverse relation between the magnitudes of the residual Burgers vector and the plastic strains across GBs. Also, the MD simulations reveal a higher energy barrier for slip transmission at high magnitudes of the residual Burgers vector. We therefore emphasize the importance of considering the magnitude of the residual Burgers vector to obtain a better description of the GB resistance to slip transmission, which in turn influences the local plastic strains in the vicinity of grain boundaries.

© 2012 Elsevier Ltd. All rights reserved.

1. Introduction

During the deformation of polycrystalline metals, some grain boundaries (GBs) act as barriers that block slip and result in dislocation pile-ups and stress concentrations (Eshelby et al., 1951; Hall, 1951; Petch, 1953). Other boundaries allow either partial or full transmission of the incident dislocations across the GB. In the case of partial dislocation transmission, a residual dislocation is left in the GB plane, and in the case of full transmission, the cross-boundary dislocation reaction takes place with no residual Burgers vector, *i.e.*, crossslip (Sutton and Balluffi, 2006). The magnitude of the residual Burgers vector at the GB plane has a predominant effect on the GB resistance against slip transmission (Lim, 1984; Lim and Raj, 1985; Lee et al., 1989).

* Corresponding author. Tel.: +1 217 3334112; fax: +1 217 2446534.

E-mail addresses: huseyin@illinois.edu, huseyin@uiuc.edu (H. Sehitoglu).

It is expected that those boundaries that are conducive to slip transmission result in low residual Burgers vectors in the GB plane and exhibit slip induced strains across both sides of the interface. In contrast, boundaries that block slip are expected to exhibit high strains in one of the grains across the interface, but relatively strain free zones in the adjacent grain. This correlation between GB resistance to slip transmission and the magnitude of plastic strains across GBs requires further quantitative investigation as it can improve our understanding of plasticity at the microstructural level and the buildup of strains that could be a precursor for damage initiation. In the present study, our aim is to develop not only a deeper understanding of strain accumulation in the vicinity of GBs within a polycrystalline aggregate, but also a *quantitative* evaluation of the resistance of GBs to slip transmission that can eventually be used in a predictive fashion. We focus on the role of slip transmission in the uniaxial plastic deformation response of the nickel-based superalloy, Hastelloy X.

The fundamental understanding of slip transmission has been developed through studies of individual GBs (Livingston and Chalmers, 1957; Shen et al., 1986; Lee et al., 1989). In these carefully conducted experimental works, different parameters were utilized to help predict the experimentally observed slip transmission reactions. Livingston and Chalmers (1957) proposed a geometric criterion for predicting specific slip system activation across a boundary due to dislocation pile-up. A modified version of this criterion was introduced by Shen et al. (1986) in which they added an additional requirement that the resolved shear stress on the outgoing, activated system had to be maximized. Lim and Raj (1985), suggested that the residual dislocation in the grain boundary plane (*i.e.*, in the case of partial transmission) plays an important role in the mechanism of slip transfer. Minimizing this residual dislocation in the boundary was later incorporated by Lee et al. (1989, 1990) as an additional criterion for slip transfer prediction (LRB criterion). An additional level of analysis was made possible through simulations at the atomic level, *e.g.*, molecular dynamics (MD) simulations. This tool provides the means for quantitative studies of the details of dislocation/GB interactions for different dislocation types and GB structures. For example, Jin et al. (2008) have explained different interaction behaviors, in addition to slip transmission, using material dependent energy barriers to nucleate partial dislocations. Dewald and Curtin (2011) have used MD simulations to formulate a modified criterion for slip transmission which incorporates, in addition to the LRB criterion, the characteristics of the GB dislocations and GB steps, and the effect of non-Schmid stresses. These kinds of simulations in conjunction with experimental work have helped develop our fundamental understanding of dislocation/GB interaction.

In the experimental studies on slip transmission, the residual Burgers vector (\mathbf{b}_r) was established using transmission electron microscopy (TEM), while in MD it was predicted from simulations that consider single dislocation/GB interaction (Ezaz et al., 2010) or a pile-up (Dewald and Curtin, 2007a, b; Dewald and Curtin, 2011). In both cases, a finite number of GBs have been considered. However, as the need to relate microstructural behavior to macroscale response through multiscale models and experiments is increasing, it will be of interest to examine such slip transmission or blockage over a much larger number of GBs than is possible in a TEM or through simulations. Therefore, for further insight into the role of \mathbf{b}_r in slip transmission and plastic strain accumulation across multiple interfaces, the consideration of a large number of GBs in a polycrystalline aggregate will be pursued in this work.

Experimental techniques such as electron backscattering diffraction (EBSD) identify grain orientations and grain boundary types (Engler and Randle, 2010), and digital image correlation (DIC) provides full-field strain measurements (Sutton et al., 1983; Efstathiou et al., 2010). Utilization of both tools to study a large ensemble of grains allows for a better quantitative understanding of the influence of GBs on the development of local strain heterogeneities during plastic deformation. In this study, high-resolution DIC is used to obtain measurements of plastic strain accumulation across GBs. This information, along with crystallographic orientation measurements from EBSD is utilized to establish the residual dislocations due to slip transmission. Based on these quantitative results, we investigate the relationship between \mathbf{b}_r and the magnitudes of strains across GBs due to slip transmission.

The material investigated in this study, Hastelloy X, is a nickel based super alloy which is designed for high temperature applications. In previous studies, researchers have investigated Hastelloy X under static (*e.g.*, Rowley and Thornton, 1996), fatigue (*e.g.*, Miner and Castelli, 1992), crack growth (*e.g.*, Huang and Pelloux, 1980) and creep loading conditions (*e.g.*, Kim et al., 2008). However, the local material response at a microstructural level has not been previously studied and will be pursued in the current work with emphasis on the slip transmission across GBs.

In summary, we seek to further investigate the role of the residual Burgers vector in slip transmission and plastic strain accumulation at the mesoscale. To accomplish this, we report the analysis of a systematic experiment (described in Section 2), in which DIC, in conjunction with EBSD, is used to interrogate deformation in the vicinity of GBs for an entire microstructure (Section 3). We establish the shear strains on crystallographic slip systems on both sides of every GB in the microstructure (*i.e.*, determine local slip system activity). From this information, regarding activated slip systems, we compute estimates of the residual Burgers vector and magnitudes of strain accumulation in the mantle regions (as defined in Section 3.2) due to slip transmission. The results reported in this study provide a better understanding of the role of GBs in mediating slip and causing local deformation heterogeneities.

2. Material and methods

2.1. Material

Commercially available polycrystalline Hastelloy X, a nickel-based superalloy, was investigated in this study. The alloy was solution heat treated by the manufacturer at 1177 °C. Dog bone specimens with 4.0 × 3.2 mm cross sectional gage area

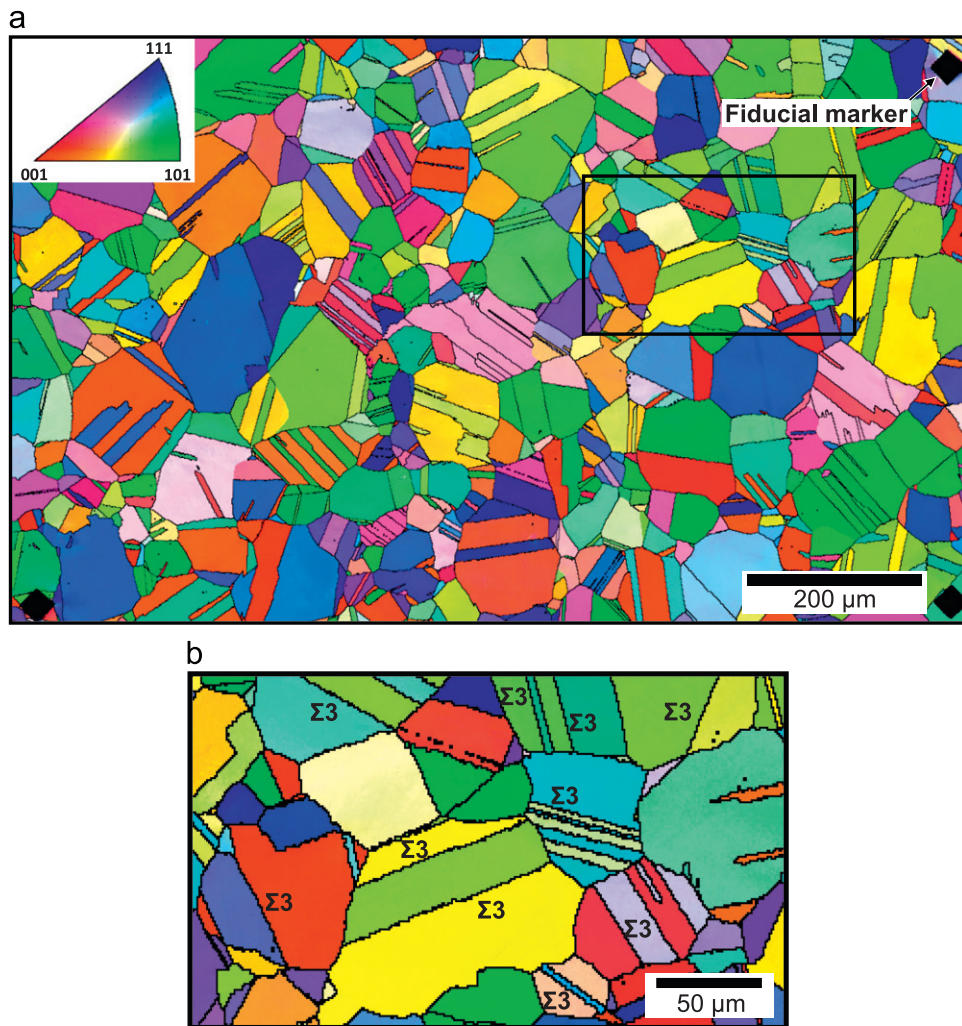


Fig. 1. (a) EBSD grain orientation map of the region of interest. Notice the fiducial markers used for outlining the region of interest. (b) Enlarged view of the region outlined with the black rectangle in (a) showing a high percentage of annealing twin boundaries ($\Sigma 3$ GBs).

were electric discharge machined from a 3.2 mm thick sheet in the as received condition. The overall sample size was selected based on the load frame loading capacity and the maximum sample size that can be investigated using the EBSD system. The surface of the specimen was mechanically polished using SiC paper (up to P1200) followed by finer polishing using alumina polishing powder (up to 0.3 μm) and vibro-polishing with colloidal silica (0.05 μm). The final surface finish was adequate for microstructural surface characterization using EBSD.

After sample preparation, a 1.0×0.6 mm region of interest was outlined on the specimen's surface using Vickers indentation marks (fiducial markers as discussed in Carroll et al. (2010)). A Scanning Electron Microscope (SEM) equipped with an EBSD detector was used to characterize the microstructure of the specimen in the region of interest. Measurement spacing of 1 μm was selected, and a total of eight area scans were necessary to cover the region of interest at the selected magnification ($300\times$). Fig. 1(a) shows a grain orientation map of the selected region of interest. No texture was observed in the aggregate consisting of approximately 600 grains. The percentage of annealing twin boundaries ($\Sigma 3$ type GBs using the coincident site lattice, CSL, notation) was about 30% of the total number of GBs, as seen in the enlarged view of Fig. 1(b).

2.2. High resolution plastic strain measurements using DIC

In DIC, images of the deformed region of interest are correlated to a reference image (of the same region prior to deformation) to make full-field measurements of displacements. Afterwards, the in-plane strain fields are calculated through differentiation of the vertical and horizontal displacement fields (Sutton et al., 1983). To obtain accurate strain measurements with sub-grain level resolution using DIC, it is necessary to increase the magnification at which reference

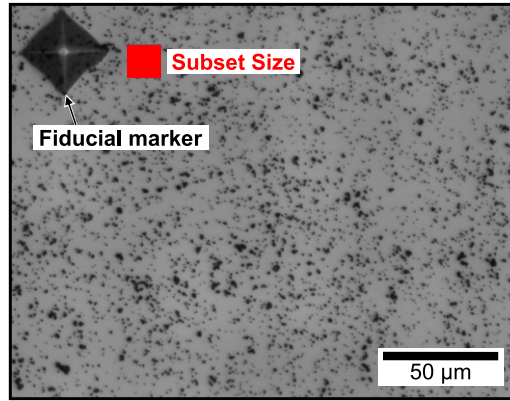


Fig. 2. A reference image captured using the optical microscope at $31\times$ magnification. The subset size and one of the fiducial markers used for alignment with microstructural information from EBSD are shown in the figure.

and deformed images are captured (Efstathiou et al., 2010). This reduces the field of view and thus imposes limitations on the area/number of grains that can be studied. The *ex situ* technique used in this study, described in detail in Carroll et al. (2010), addresses this problem and enables high resolution measurements over relatively large areas by capturing and stitching enough high magnification images to cover the required region of interest.

Following EBSD, a fine speckle pattern was applied to the sample's surface for DIC measurements. Reference images were captured using an optical microscope at $31\times$ magnification ($0.14\ \mu\text{m}/\text{pixel}$). Fig. 2 shows an example of a reference image with the speckle pattern and subset size (101×101 pixels) used in the current work. A total of 316 overlapping images were required to cover the region of interest outlined by the indentation marks. These reference images were stitched together to generate one ultra-high resolution reference image that covered the complete region of interest. The specimen was then deformed in uniaxial tension using a servo-hydraulic load frame to 2.2% nominal strain (using strain control at $1.83\times 10^{-4}\ \text{s}^{-1}$ strain rate) and unloaded (using load control). After unloading, the total residual strain was 2% nominal strain measured using a 12.7 mm ($1/2''$) gage length extensometer. Subsequently, 316 deformed images were captured and stitched, following the same procedure used for the reference images. In plane displacements were obtained from DIC and the results were differentiated to obtain the high resolution strain fields. The subset size used for DIC ($14\ \mu\text{m}$) is smaller than the average grain size ($50\ \mu\text{m}$) allowing for sub-grain level deformation measurement resolution (average number of DIC correlation points per grain=350). The fiducial markers visible in both the EBSD orientation map and DIC contour plots, allow for accurate alignment of the measured strain fields and the underlying microstructure in the region of interest (Carroll et al., 2010). The advantage of such a measurement procedure is that it enables quantitative analysis of the plastic strain fields in relation to the underlying microstructure of the polycrystalline specimen. Different aspects of the microstructure, such as GBs and grain orientation, coupled with their influence on plastic strain accumulation were investigated using this technique.

3. Results and analysis

3.1. Local plastic strain

Fig. 3(a)–(c) show the contour plots of the horizontal strain field ε_{xx} , the shear strain field ε_{xy} , and vertical strain field ε_{yy} (along the loading direction). These components of the strain tensor were acquired using DIC. By assuming plastic incompressibility, the component in the residual plastic normal strain along the third direction, ε_{zz} , was calculated using

$$\varepsilon_{zz} = -1 \times (\varepsilon_{xx} + \varepsilon_{yy}). \quad (1)$$

The shear strain components in the third direction, ε_{xz} and ε_{yz} remain unknown in our analysis (as in any surface measurement technique). Using the measured and calculated components of the plastic strain tensor and by assuming the unknown components as zero, an estimate of the effective plastic strain, $\varepsilon_{\text{eff}}^p$, was calculated spatially using the following equation:

$$\varepsilon_{\text{eff}}^p = \sqrt{\frac{2}{3}(\varepsilon_{ij} \times \varepsilon_{ij})}. \quad (2)$$

To assess and analyze the effect of microstructure, local crystallographic orientations from EBSD were numerically overlaid on the DIC strain data, i.e., for each point, spatial strain and orientation data were consolidated. Eventually, each point in the field has four components of the strain tensor (ε_{xx} , ε_{yy} , ε_{xy} , and ε_{zz}), the effective plastic strain, and an associated local crystallographic orientation. This allowed for a superposition of the grain boundaries on all the strain contour plots as shown for example for the ε_{yy} in Fig. 3(c).

A significant level of heterogeneity is observed from the strain contour plots. In Fig. 3(c), regions rendered in dark red have strains higher than 3% (ϵ_{yy} field average = 2%), while regions rendered in dark blue have strains around 0%, and some are even negative, *i.e.*, compressive, in certain areas. This variation in strain appears to be associated with the local microstructure. For example, high strains were visually detected in the vicinity of many grain boundaries (Fig. 3(d)). In the next section, we quantitatively assess the correlation between the presence of GBs and the local heterogeneities in the plastic strains.

3.2. Grain boundary mantles

Full-field strain measurements at the grain level enable us to address the specific regions of grains, which facilitate accumulation of heterogeneous strains. This is accomplished through separating each grain into a core and mantle demarcation utilizing the combination of high resolution DIC and EBSD. The core refers to the interior of the grain and the

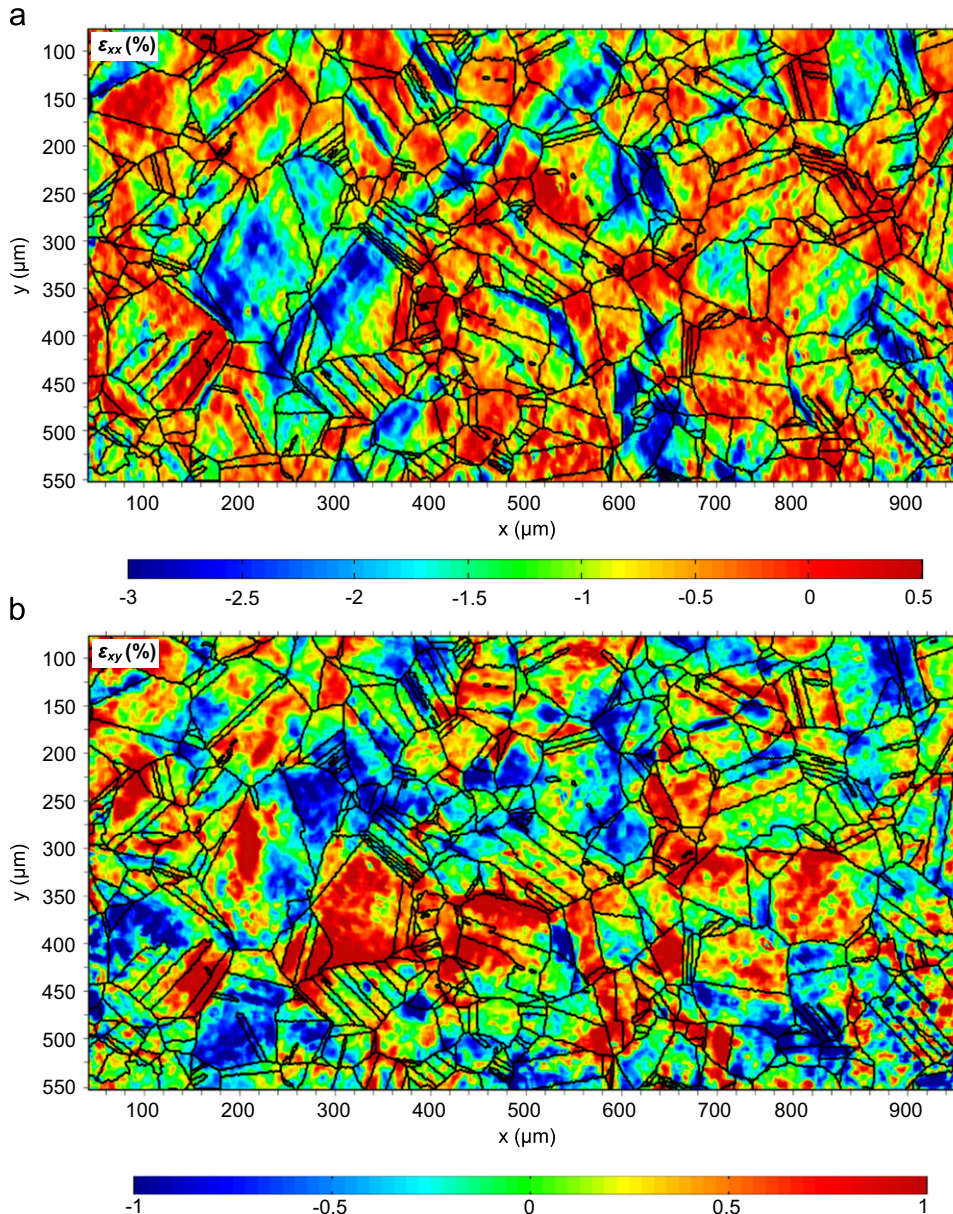


Fig. 3. (a)–(c) Contour plot of the horizontal (ϵ_{xx}), shear (ϵ_{xy}), and vertical (ϵ_{yy}) strain fields with overlaid grain boundaries. The reference and deformed images for DIC are a composite of 316 images at $31\times$ magnification (*exsitu*). (d) Enlarged view of the region outlined with the black rectangle in (c). The red box in the upper left corner shows the subset size used for this correlation. Note that the subset size is much smaller than the average grain size providing sub-grain level measurement accuracy. High strains can be detected in the vicinity of grain boundaries (some indicated with black arrows). GB character is shown for some boundaries, where IR indicates irrational GBs.

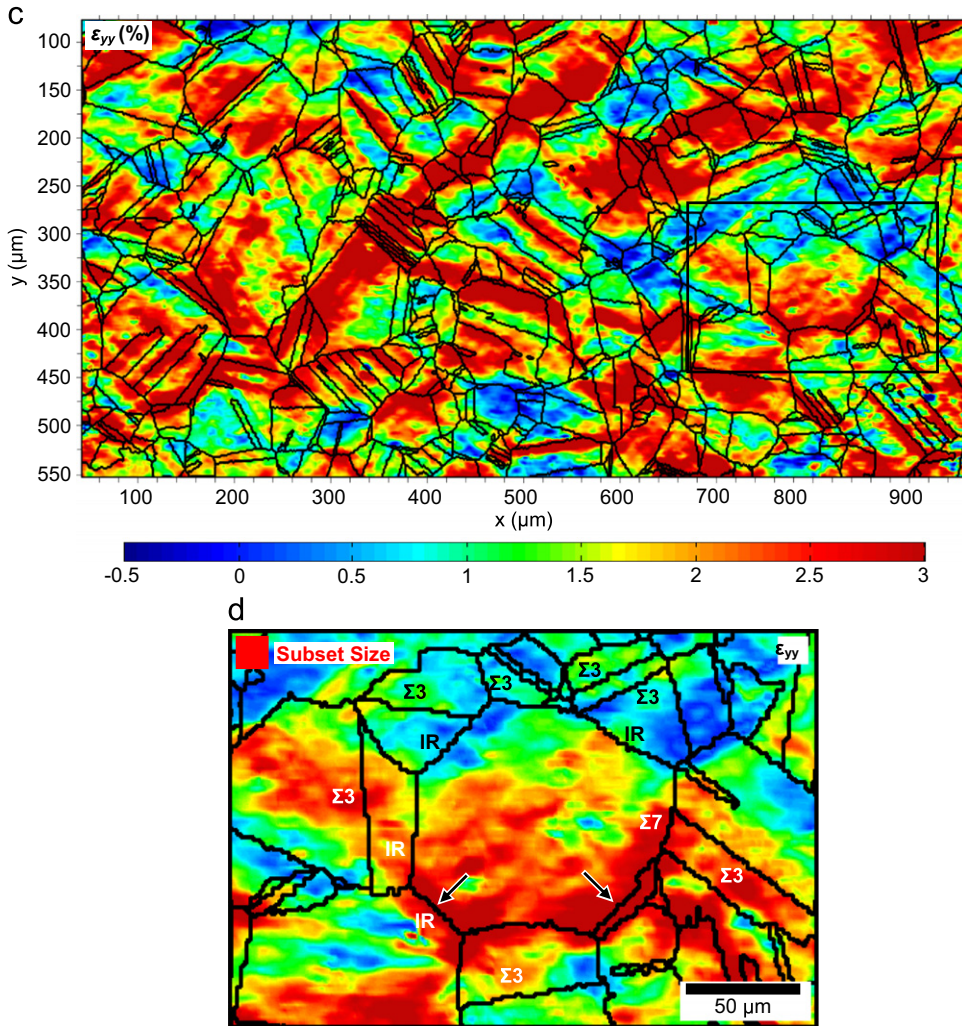


Fig. 3. (continued)

mantle to the region in the vicinity of the neighboring grain, *i.e.*, the region of the grain near the GB (Meyers and Ashworth, 1982). Hence, each grain has several mantles corresponding to the number of neighboring grains. Mantle regions, which exhibit high strains on both sides of the interface, can be associated with slip transmission across the GB, while boundaries that block slip, *i.e.*, shielding, have high strains in one of the mantles and low strains in the other mantle across the interface.

In this section, we establish an experimental estimate of the GB mantle size from DIC strain measurements and grain boundary locations. To do so, we calculated the spatial distance from each DIC measurement point to the nearest grain boundary, as shown schematically in the inset of Fig. 4(a). This facilitates binning the strain data based on distance from the GBs. As the focus in this study is on high strain regions that can be associated with slip transmission across GBs, only points with high strains were considered ($> \epsilon_{\text{eff}}^p$ field average = 2.08%). These points were then binned based on their distance from the nearest GB, and the average strain in each bin was computed. Fig. 4(a) shows a plot of the average effective plastic strain ϵ_{eff}^p versus distance from the closest boundary (only points $> \epsilon_{\text{eff}}^p$ field average = 2.08% were considered in this figure). We observe that the magnitude of the elevated strains decrease as we move away from the GBs (mantle regions) and approach the grain interior regions (core).

At a distance of $\sim 10 \mu\text{m}$ from the boundary, there is an inflection point in the change of strain with respect to distance from the GB as observed from the change in slope of the black dashed lines in Fig. 4(a). This point was used as an experimentally measured estimate of the GB mantle size, since it marks a transition in slip response while moving away from the GB and approaching the core of the grain. Once the mantle size was determined, mantle points were selected for each specific boundary across the *entire* microstructure, *i.e.*, select points within $10 \mu\text{m}$ from the GBs. Each GB has two mantles associated with it; one on each side of the GB across the interface. Fig. 4(b) shows an example of GB mantles defined in this work. Delineating the mantle regions helps in determining the core points for each specific grain by subtracting all the mantle points from the total number of points in each grain.

Strain histograms of ϵ_{eff}^p in cores and mantles over the entire microstructure in the area of interest, approximately 600 grains, are shown in Fig. 5. The histogram of the points belonging to mantles, *i.e.*, red histogram, shows a range of strains

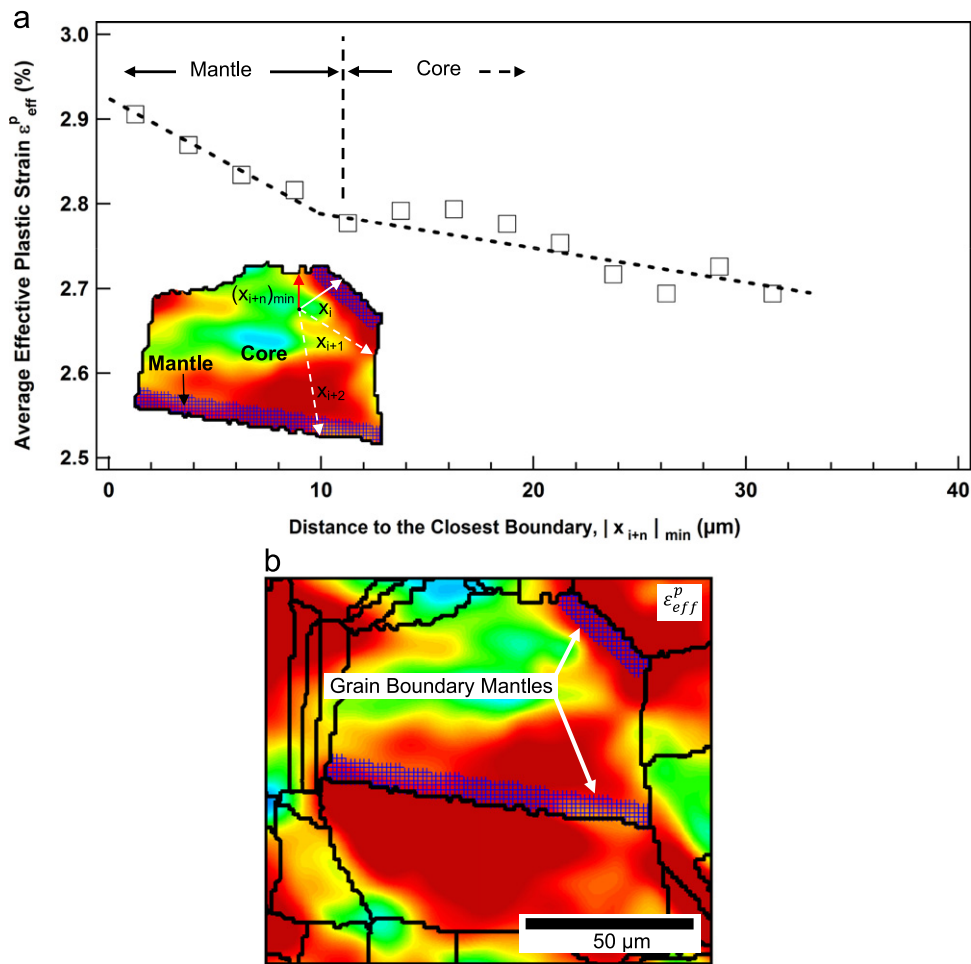


Fig. 4. (a) Average effective plastic strain ε_{eff}^p versus distance from the closest boundary (only high strain points were considered). For each point in the region of interest the distance to the closest GB is measured as shown schematically for a single point in the inset of (a). The data points were then binned based on their distance from the nearest boundary (x axis). The y axis represents the average strain in each distance bin. The figure indicates that high strains localize in the vicinity of the boundary (GB mantle) and that the degree of localization decreases as we move away from the boundary (core of the grain). At $\sim 10 \mu\text{m}$ distance from the boundary, the rate of this decrease changes as observed by the change in slope of the black dashed line. This point was used as an estimate of the GB mantle size as it marks a transition in response as we move away from the GB and approach the core of the grain. (b) Examples showing the experimentally defined GB mantles.

between 0 and 6%, while points belonging to cores, *i.e.*, black histogram, show a smaller strain range between 0.1 and 4.2%. Less scatter around the mean was also observed for the core histogram (standard deviation=0.8) compared to mantle histogram (standard deviation=0.9). We also notice in Fig. 5 that the mean strain for mantle points (2.05%) is less than the mean strain for core points (2.18%). This is primarily attributed to the low strains in some of the mantle regions which lower the mean strain of the mantle points. We emphasize that the presence of mantle points with low strains does not contradict the results presented in Fig. 4(a) as only points with relatively high strains were used to construct that figure as opposed to considering all the points, regardless of their magnitude, in the results presented in Fig. 5.

As seen from the inset image on the right side of Fig. 5, some of the highly strained regions extend across the boundary into the neighboring grain and show continuous slip traces across the GBs as shown, for example, in Fig. 6. This can be an indication of slip transmission across the boundary (transmitting mantles). Other regions (inset images on the left side of Fig. 5) show high strains on only one side of the GB and relatively low strains on the other side. This case can be associated with blockage or shielding (shielding mantle). All the GBs in the region of interest were individually interrogated and classified as either shielding or transmitting GBs based on the strain magnitudes measured in mantle regions across each interface. For the study of slip transmission, we focused our analysis *only on the transmitting mantles*, which exhibit high strains on both sides of the GB.

3.3. Local slip system activity

In order to establish estimates of the residual Burgers vector due to slip transmission, additional information regarding the crystallographic slip systems involved in the transmission process is required. Traditionally, determining the active slip

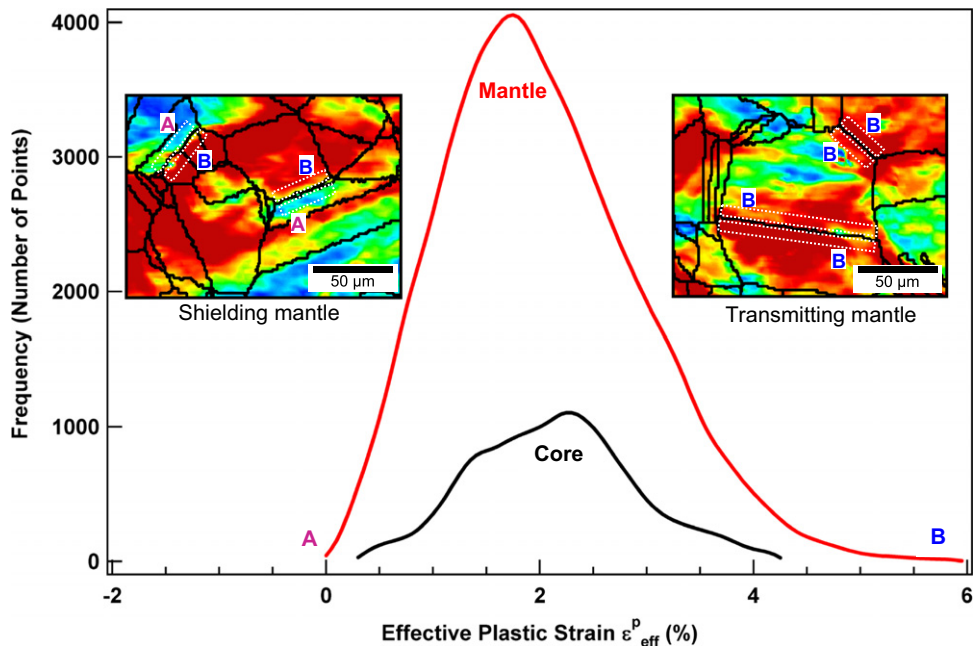


Fig. 5. Histograms of the effective plastic strains $\varepsilon_{\text{eff}}^p$ for points in mantles (red histogram) and cores (black histogram). The histogram of points belonging to mantles shows a wide range of strains between 0 and 6%. The contour plot to right shows high strains in both mantles across the boundary. This can be an indication of slip transmission across the boundary (Transmitting mantles. See also Fig. 6). Other regions show high strains in only one of the mantles across the GB and relatively zero strains on the other side. This case can be associated blockage or shielding (Shielding mantle). The histogram of the points belonging to cores, i.e., black histogram, shows a smaller strain range between 0.1 and 4.2%. Less scatter around the mean is also observed for the core histogram (standard deviation=0.8) compared to mantle histogram (standard deviation=0.9).

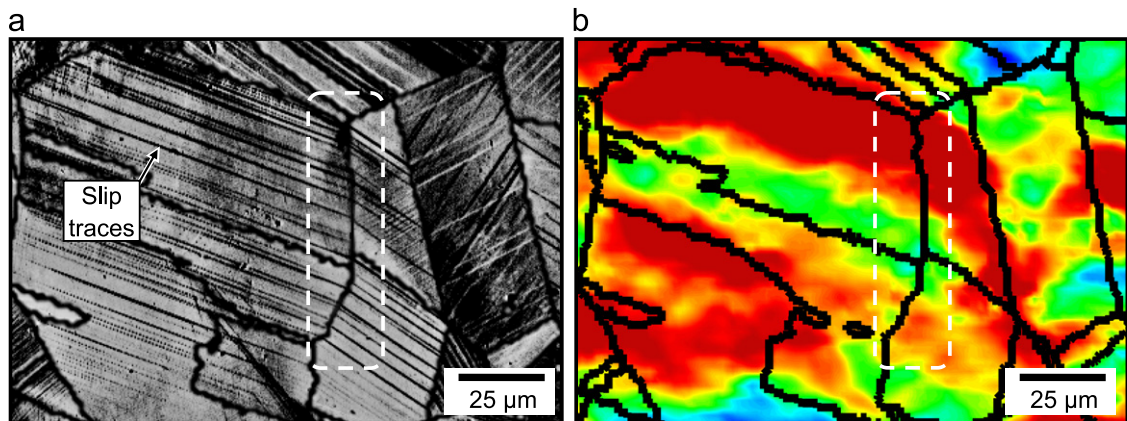


Fig. 6. (a) SEM micrograph of a select region showing continuous slip traces across multiple GBs. This can be an indication of slip transmission across the boundary. (b) Contour plot of ε_{yy} showing high strains across the GBs with continuous slip traces (i.e., transmitting mantles). (For interpretation of the references to color in this figure legend, the reader is referred to the web version of this article.)

systems from experiments has been accomplished through a combination of slip trace analysis and Schmid factor calculations (Zhang and Tong, 2004; Zhao et al., 2008; Bartali et al., 2009; Bieler et al., 2009). A different method for determining the active slip systems utilizes the measured local plastic strains and crystal orientation to solve for the crystallographic shear strains (Tatschl and Kolednik, 2003). Results utilizing both of these approaches are presented in Sections 3.3.1 and 3.3.2, respectively.

3.3.1. Slip trace analysis

In fcc materials, 12 possible slip systems exist; three $\{1\ 1\ 0\}$ directions on each of four $\{1\ 1\ 1\}$ planes. An activated slip system creates a slip trace on the sample's surface (provided that the slip plane of that system is not parallel to the sample's surface). Observing and identifying the slip systems associated with the slip traces is used to determine the activated slip systems. Slip traces are seen from SEM micrographs as shown in Fig. 7 (for the same region shown earlier in Fig. 3(d)).

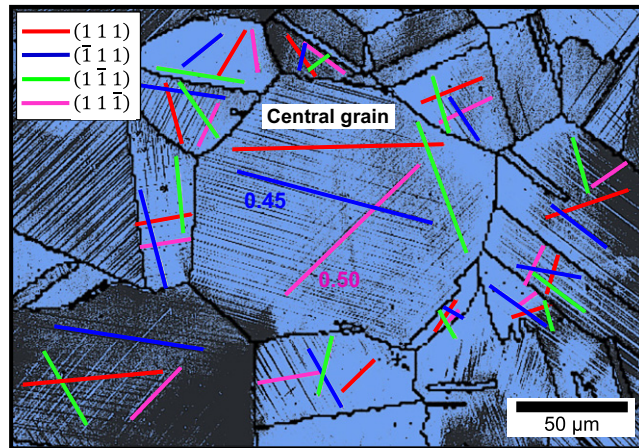


Fig. 7. SEM micrograph of the deformed sample showing traces of the activated slip systems (same region outlined in Fig. 3(d)). Possible traces of crystallographic slip planes can be specified on the sample's surface using the local orientation data obtained from EBSD. Each colored line represents a different slip plane (fcc $\{1\ 1\ 1\}$ slip planes). By matching the observed slip traces with the possible traces (*i.e.*, colored lines), the activated slip planes can be specified. The numbers written next to two of the slip traces in the central grain represent the Schmid factors of the slip systems with the highest Schmid factor for the observed traces. (For interpretation of the references to color in this figure legend, the reader is referred to the web version of this article.)

Table 1

Schmid factors of the 12 slip systems for the central grain shown in Fig. 7 (see Appendix for details on Schmid factor calculation).

Slip system, α	Slip plane	Slip direction	Schmid factor
System 1	(1 1 1)	$[1\ \bar{1}\ 0]$	0.12
System 2	(1 1 1)	$[1\ 0\ \bar{1}]$	0.15
System 3	(1 1 1)	$[0\ 1\ \bar{1}]$	0.04
System 4	($\bar{1}\ 1\ 1$)	$[1\ 0\ 1]$	0.25
System 5	($\bar{1}\ 1\ 1$)	$[0\ 1\ \bar{1}]$	0.20
System 6	($\bar{1}\ 1\ 1$)	$[1\ 1\ 0]$	0.45
System 7	($\bar{1}\ \bar{1}\ 1$)	$[\bar{1}\ 0\ 1]$	0.30
System 8	($\bar{1}\ \bar{1}\ 1$)	$[0\ 1\ 1]$	0.13
System 9	($\bar{1}\ \bar{1}\ 1$)	$[1\ 1\ 0]$	0.17
System 10	($1\ 1\ \bar{1}$)	$[1\ \bar{1}\ 0]$	0.50
System 11	($1\ 1\ \bar{1}$)	$[1\ 0\ 1]$	0.20
System 12	($1\ 1\ \bar{1}$)	$[0\ 1\ 1]$	0.29

We used the crystal orientation measurements from EBSD to determine the slip planes, *not* systems, associated with the observed traces. The procedure involves rotating the slip plane normal vectors, \mathbf{n} , from crystal frame to sample frame, and then finding the intersection of the slip planes (define by the resulting normal vectors in sample frame) with the sample's surface (Engler and Randle, 2010). These intersections represent the possible traces of slip planes (colored lines in Fig. 7). Matching of a possible slip trace with an observed one confirms the activation of that slip plane. For example, the central grain in Fig. 7 shows clear activation of the ($\bar{1}\ 1\ 1$) slip plane (blue line) and the ($1\ 1\ \bar{1}$) plane (magenta line). Schmid factors were used to make further specification regarding the slip directions associated with these slip planes.

Table 1 lists the Schmid factors of the 12 slip systems for the central grain in Fig. 7 (uniaxial loading conditions in the vertical direction). Systems 6 and 10 have the highest Schmid factors and, thus, they are the most likely to be activated compared to other systems with lower Schmid factors. This is the most probable case for the grain under consideration since these systems are on the ($\bar{1}\ 1\ 1$) and the ($1\ 1\ \bar{1}$) slip planes, which are active from slip traces. Obviously, this approach does not provide quantitative information regarding the degree of slip activity in each system. Also, the spatial differences in slip system activation leading to the heterogeneities within grains, observed in Fig. 3(d), can not be detected or quantitatively measured. This calls for a better global approach capable of extracting slip system activation *quantitatively* across the entire region of interest. In the next section, an alternative method, which provides local information about slip system activation, *e.g.*, in GB mantles, is presented.

3.3.2. Crystallographic shear strain increments

The local change in the plastic strain, due to crystallographic slip, is achieved through increments of shear, $d\gamma^\alpha$, in the activated slip systems (Kocks and Chandra, 1982). The individual components of the plastic strain tensor are given by the

following equation:

$$de_{ij}^p = \frac{1}{2} \sum_{\alpha=1}^s (n_i^\alpha l_j^\alpha + n_j^\alpha l_i^\alpha) d\gamma^\alpha = \sum_{\alpha=1}^s (m_{ij}^\alpha) d\gamma^\alpha, \quad (3)$$

where α is the slip system number (see Table 1 for planes and directions), s is the number of slip systems (12 for fcc), n^α is the vector defining the normal to slip plane for system α , and l^α is the vector defining the slip direction. Three components of the plastic strain tensor were measured from DIC (ϵ_{xx} , ϵ_{yy} , ϵ_{xy}). The fourth component, ϵ_{zz} , was calculated by assuming plastic incompressibility (Eq. (1)). Also, n^α and l^α are known for fcc crystals (as shown in Table 1). Solving for the scalar quantities $d\gamma^\alpha$ at each spatial point provides local information about slip system activation across the entire region of interest.

The problem that arises when attempting to solve Eq. (3) is that the number of activated slip systems is not generally known. Also, if the number of activated systems is assumed, five has been proposed as sufficient number of systems necessary to satisfy compatibility (Taylor, 1938), the problem of which combination to select from the twelve possible systems arises. Taylor proposed a model to solve this problem. In his formulation, the combination which minimizes the sum of the absolute values of the shear increments is considered to be the combination that is actually operative (Taylor, 1938). Since then, different models and constitutive formulations, that are more physically based, have been proposed to solve this problem (Roters et al., 2010). In the current work, a visco-plastic constitutive model was used to solve for the shear strain increments spatially across the entire microstructure. In the formulation used, which is standard in many crystal plasticity frameworks, the shear strain rate is written as a function of the resolved shear stress on each slip system (Hutchinson, 1976):

$$\frac{\dot{\gamma}^\alpha}{\dot{\gamma}_0} = \left| \frac{\tau^\alpha}{\bar{\tau}} \right|^n \text{sgn}(\tau^\alpha) \quad (4)$$

where $\dot{\gamma}^\alpha$ is the shear rate on slip system α , τ^α is the resolved shear stress, $\bar{\tau}$ is a reference stress state, and $\dot{\gamma}_0$ and n are material parameters that describe the reference strain rate and the slip rate sensitivity, respectively. The term “ $\text{sgn}(\tau^\alpha)$ ” in Eq. (4) is present in order to ensure that $\dot{\gamma}^\alpha$ and τ^α have the same sign (*i.e.*, positive work is being done). Eq. (4) can be rewritten as follows:

$$\dot{\gamma}^\alpha = \frac{\dot{\gamma}_0}{\bar{\tau}} \left| \frac{\tau^\alpha}{\bar{\tau}} \right|^{n-1} \tau^\alpha. \quad (5)$$

As the emphasis in our analysis is to obtain the shear strain increments, $d\gamma^\alpha$, and not solving for the exact kinetics, *i.e.*, the shear stress τ^α , we take $\dot{\gamma}_0 = \bar{\tau} = 1$ and $n=20$, *i.e.*, rate insensitive.

If we make the simplification that $d\gamma^\alpha = \dot{\gamma}^\alpha$, we can substitute for the shear increments from Eq. (5) into the net strain Eq. (3), producing a relation between the total plastic strain and resolved shear stresses

$$\dot{e}_{ij}^p = \sum_{\alpha=1}^s \left(\frac{\dot{\gamma}_0}{\bar{\tau}} \left| \frac{\tau^\alpha}{\bar{\tau}} \right|^{n-1} \tau^\alpha \right) (m_{ij}^\alpha). \quad (6)$$

The resolved shear stress on each slip system (τ^α) is related to the stress tensor (σ_{ij}) through the following equation:

$$\tau^\alpha = m_{pq}^\alpha \sigma_{pq}. \quad (7)$$

Substituting Eq. (7) into Eq. (6):

$$\dot{e}_{ij}^p = \left[\sum_{\alpha=1}^s \left(\frac{\dot{\gamma}_0}{\bar{\tau}} \left| \frac{\tau^\alpha}{\bar{\tau}} \right|^{n-1} m_{ij}^\alpha m_{pq}^\alpha \right) \right] \sigma_{pq}. \quad (8)$$

Given the local plastic strain rate (here we make the simplification that $\dot{e}_{ij}^p = de_{ij}^p$) and the orientation data (to be able to transform from sample frame to crystal frame) we solved Eq. (8) – the non-linear system of equations was solved using an iterative solver – for the stresses σ_{pq} . Subsequently, the resolved shear stresses τ^α were calculated using Eq. (7). Finally, Eq. (5) was used to back-substitute for the shear strain rates. Following this procedure, the shear strain increments can be specified on all the 12 slip systems (*i.e.*, no question of choosing the active slip systems arises; all systems with nonvanishing resolved shear stress are potentially active). By performing this calculation for each spatial point across the region of interest, we acquired spatial information about slip system activation across the entire microstructure.

An example of the results obtained using this procedure is shown in Fig. 8(a), which depicts a contour surface plot of the crystallographic shear strain increment on system 10 across the entire region of interest, *i.e.*, $|d\gamma^{10}|$ on $(11\bar{1})[1\bar{1}0]$ slip system. Note that the direction of slip system 10 in sample coordinates is different for each grain depending on its orientation. In Fig. 8, the dark blue color indicates no activity of that particular slip system, while the red color indicates slip system activation. For better visualization, an enlarged view of a particular sub-region is shown in Fig. 8(b). Compared to the slip trace analysis, this approach offers a quantitative description of activation on the slip system level with spatial information capable of capturing differences within a single grain or cluster of grains across the entire aggregate. This is important for our slip transmission analysis, since we wish to focus on slip activity in mantle regions.

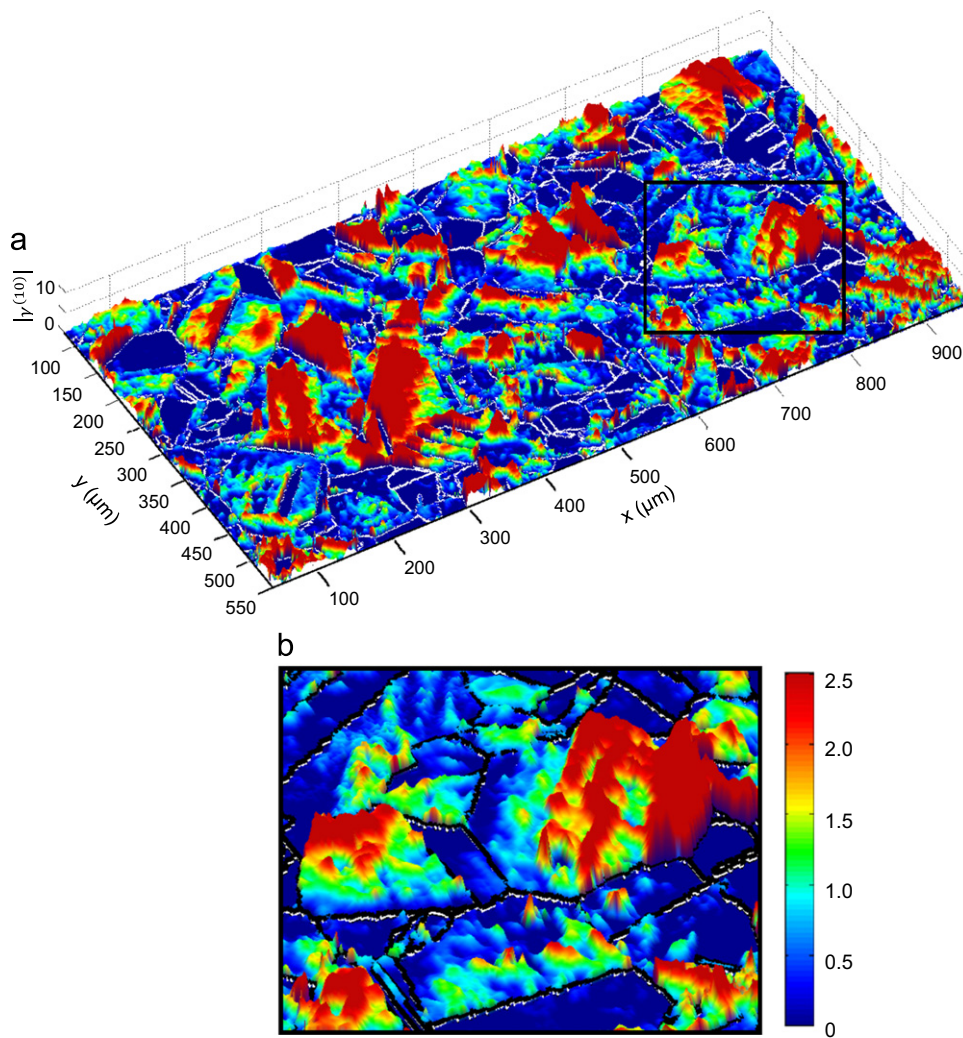


Fig. 8. (a) Contour plot of the crystallographic shear increment on system 10 across the entire region of interest ($|d\gamma^{10}|$ on $(11\bar{1})[1\bar{1}0]$ slip system). The dark blue color indicates no activity of that particular slip system while red colored regions indicate slip system activation. (b) An enlarged view of the smaller region outlined in (a) is shown for better visualization.

Contour plots similar to Fig. 8(a) were generated for the other eleven slip systems. For the sake of brevity, in Fig. 9, we only show the ones with the highest shear increments in the same region shown earlier in Figs. 3(d) and 7. Different slip systems were activated in various spatial regions of the central grain, while certain slip systems, such as 5 and 8, show activity only in the vicinity of some grain boundaries, *i.e.*, mantle regions. This spatial information, regarding activated slip systems on both sides of every grain boundary in the region of interest (approximately 1600 GBs), along with crystallographic grain orientation was used to provide insight into the local deformation behavior in grain boundary regions. In the next section, this information is used to study the role of the residual Burgers vector in slip transmission and strain accumulation across grain boundaries.

3.4. Residual Burgers vector

As previously mentioned, one of the possible outcomes of dislocation-grain boundary interaction is partial slip transmission of the incoming slip across the GB, which leaves behind a residual dislocation in the GB plane. The following dislocation reaction equation is used to define \mathbf{b}_r based on the Burgers vectors of the dislocations on both sides of the GB (Sutton and Balluffi, 2006):

$$\vec{\mathbf{b}}_r = \vec{\mathbf{b}}_1 - \vec{\mathbf{b}}_2, \quad (9)$$

where \mathbf{b}_1 and \mathbf{b}_2 are the Burgers vectors of the incident and transmitted dislocations across the GB, respectively (see schematic in Fig. 10). When information about these quantities is lacking, *i.e.*, we do not know the exact types of the

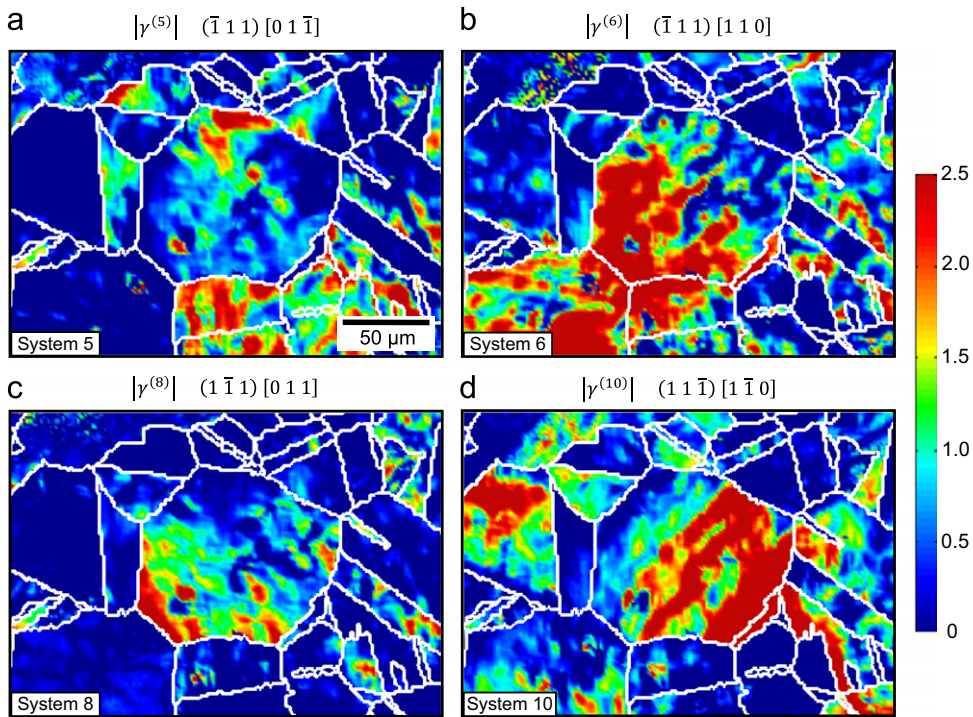


Fig. 9. (a)–(d) Contour plot of the crystallographic shear increments in the region outlined with the black box in Fig. 3(c). Only the highest 4 activated systems are shown for increased clarity (systems 5, 6, 8 and 10). Different slip system activity in different regions of the central grain is clearly seen. Some systems are only activated in the vicinity of some grain boundaries (e.g., systems 5 and 8).

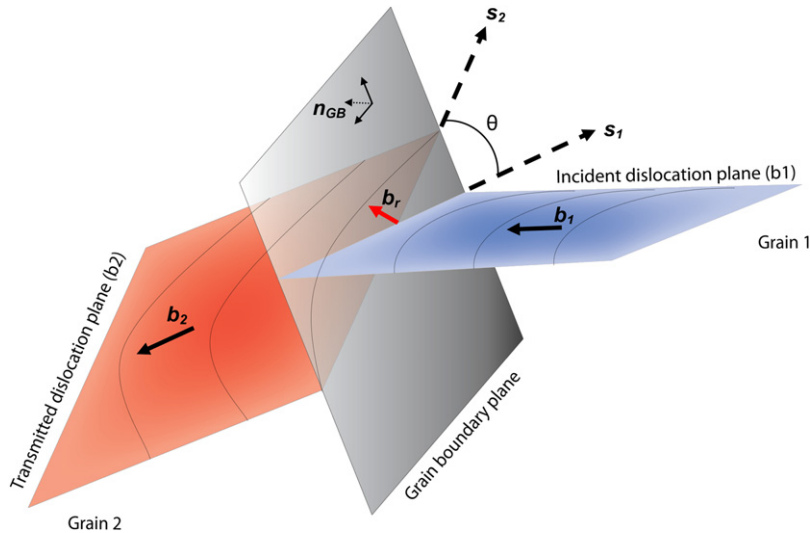


Fig. 10. Schematic of slip transmission through a grain boundary, where \mathbf{b}_1 and \mathbf{b}_2 are the Burgers vector of the incident and transmitted dislocations across the GB plane. Also, θ is the angle between the lines of intersection between slip planes of the incident and transmitted dislocations and the GB plane. \mathbf{b}_r is the residual dislocation left in the GB plane due to slip transmission.

incident and transmitted dislocations, the difference between the slip directions (l_1 and l_2) can be used as an approximation of the magnitude of \mathbf{b}_r

$$|\vec{\mathbf{b}}_r| = |\vec{\mathbf{l}}_1 - \vec{\mathbf{l}}_2|. \quad (10)$$

In the most general case, 144 possible interactions exist for slip transmission at each GB. This number of possible interactions is obtained by considering the 12 slip systems (fcc material) within grain 1 (incident) and 12 slip systems within grain 2 (transmitted). Note that the same reaction is obtained by reversing the order of the incoming and outgoing

dislocations (considering the magnitude of \mathbf{b}_r). For example, if slip system 1 is the incident slip system in the first grain and slip system 2 is the transmitted slip system in the other grain across the GB, then the magnitude of the residual Burgers vector resulting from this interaction (Eq. (10)) will be similar to the reaction obtained if the order of incident and transmitted slip is reversed, *i.e.*, slip system 2 in the second grain becomes incident and system 1 becomes transmitted. Notice that this order reversal of the incident and transmitted slip systems implies reversing the slip directions of both systems involved in the transmission process, *e.g.*, if the slip direction l_1 is incident slip for a GB, then $-l_1$ is transmitted slip for the same boundary. To specify whether a slip system is incident or transmitted relative to a specific GB, we check the sign of the inner product between the slip direction and the vector defining the normal to the GB plane (\mathbf{n}_{GB}). If \mathbf{n}_{GB} is defined as shown in Fig. 10, then a positive inner product between the slip direction of the slip system in Grain 1 and \mathbf{n}_{GB} indicates that the slip direction is incident relative to that GB and a negative inner product indicates that it is transmitted. We therefore check and adjust the signs of the slip directions (slip directions are shown in Table 1 for fcc crystals) for each of the possible slip transmission interactions to guarantee that one of the systems is incident and the other transmitted relative to the GB under consideration.

In our analysis, we have individually selected each GB and interrogated the 144 possible slip transmission interactions by checking if both of the slip systems associated with each interaction were activated in the mantle regions of that GB. In the case of confirmed activation of both slip systems, through the DIC strain measurements, an experimental estimate of \mathbf{b}_r was calculated for that specific GB. If multiple slip systems were activated in the mantles, several estimates of \mathbf{b}_r were calculated. Fig. 11 shows two of these possible interactions for a transmitting mantle case. In this figure, the magnitude of the residual Burgers vector and the grain boundary Schmid factor parameter are shown for each of the two possible interactions. The plotted parameters are defined using the following equations:

$$Sch^{(\alpha,\beta)} = Sch_{incident}^{\alpha} + Sch_{transmitted}^{\beta} \quad (11)$$

$$|b_r^{(\alpha,\beta)}| = |l_{incident}^{\alpha} - l_{transmitted}^{\beta}|, \quad (12)$$

where $Sch^{(\alpha,\beta)}$ is the GB Schmid factor parameter, $Sch_{incident}^{\alpha}$ is the Schmid factor of slip system α (of incident dislocation), $Sch_{transmitted}^{\beta}$ is the Schmid factor of slip system β (of transmitted dislocation), and $|b_r^{(\alpha,\beta)}|$ is the magnitude of the residual Burgers vector from the interaction that involves incident dislocations on system α and transmitted dislocations on slip system β .

One of the cases plotted in Fig. 11 has a high GB Schmid factor parameter and a relatively low $|b_r|$ (the point on the left side of the figure). This interaction represents slip system 6 being activated in both grains across the GB (notice that although both systems are 6, they have different orientations in the sample frame). The contour plots of the shear strains show activation of systems 6 in mantle regions across the GB. The activation of both slip systems associated with this interaction point is considered an indication of slip transmission across the GB. The point to the right in Fig. 11 represents the interaction between systems 6 and 7. Even though the value of the Schmid factor parameter is high, no activation of

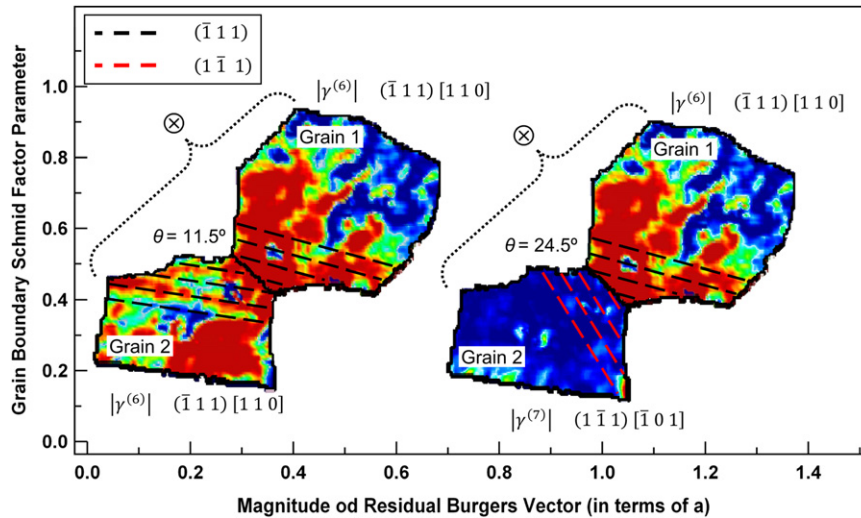


Fig. 11. Grain boundary Schmid factor parameter *versus* residual Burgers vector. The point to the left represents the interaction between slip system 6 in grain 1 and system 6 in grain 2. The contour plots of the shear increments show activation of systems 6 in mantle regions across the GB. The activation of both slip systems associated with this interaction point is considered an indication of slip transmission across the GB. The point to the right represents the interaction between systems 6 and 7. No transmission from system 6 in grain 1 to system 7 in grain 2. Notice the high residual Burgers vector associated with this possible interaction. Also, the geometric condition θ for this interaction is larger than the point to the left where transmission is observed ($\theta^{6,7} = 24.5^\circ > \theta^{6,6} = 11.5^\circ$). This makes transmission less favorable due to the larger misalignment of slip planes. This can be visualized by looking at the possible slip traces for each slip system in both grains (dashed black line for system 6 and red for system 7).

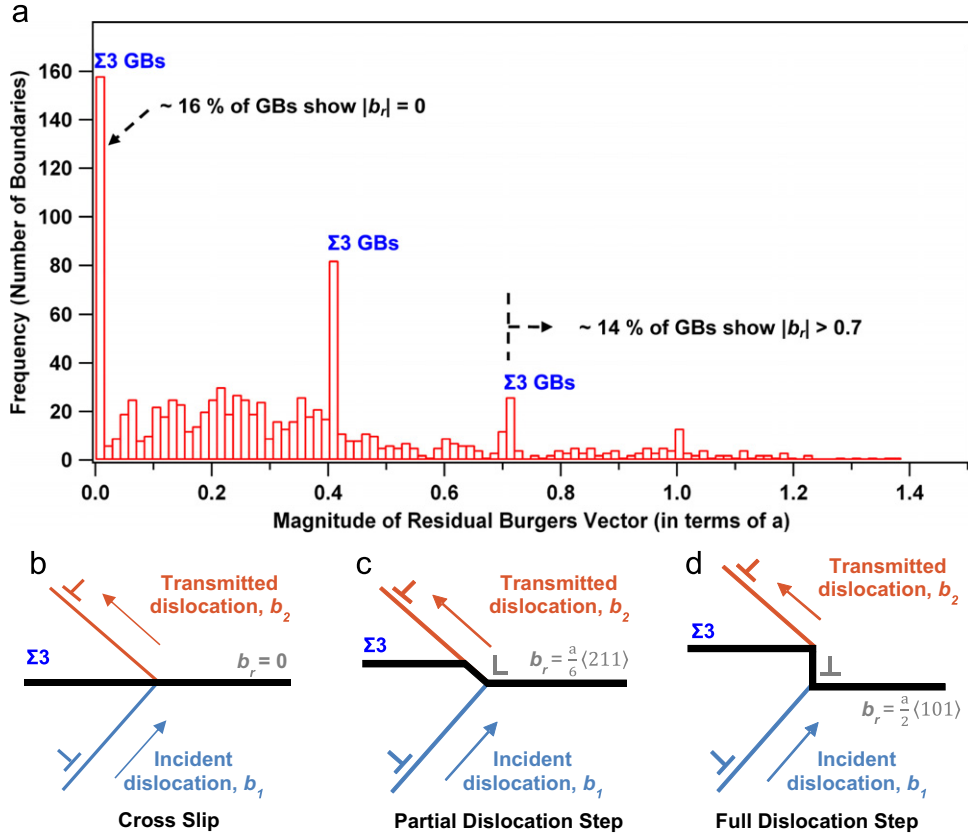


Fig. 12. (a) Histogram of the minimum $|b_r|$ for each of the transmitting GBs in the region of interest (~ 1000 GBs). Notice that some of the transmission cases occur leaving relatively high magnitudes of b_r , e.g., 14% of GBs show $|b_r| > 0.7$. Three distinct spikes in the number of GBs having similar $|b_r|$ can be observed at $|b_r| = 0$, $|b_r| = 0.41$, and $|b_r| = 0.71$. Most of these boundaries were characterized as $\Sigma 3$ type. The first spike is at $|b_r| = 0$, this represent cross slip leaving no residual in the GB plane as shown schematically in (b). The second spike is at $|b_r| = |(a/6) < 211 >| = a/\sqrt{6}$; this reaction leaves a partial dislocation step in the GB plane as shown in (c). The third spike is at $|b_r| = |(a/2) < 101 >| = a/\sqrt{2}$, which leaves a full dislocation step in the GB plane as shown in (d).

system 7 in grain 2 was observed, i.e., no transmission from system 6 in grain 1 to system 7 in grain 2. Notice the high magnitude of the residual Burgers vector associated with this possible interaction. Also, the geometric condition, θ , which describes the angle between the lines of intersection between slip planes of the incident and transmitted dislocations and the GB plane (shown in Fig. 10), for systems 6 and 7 is larger than the geometric condition for systems 6 and 6, where transmission is observed ($\theta^{6,7} = 24.5^\circ > \theta^{6,6} = 11.5^\circ$). This makes transmission less favorable due to larger misalignment between slip planes. The active slip systems, experimentally determined from DIC strain measurements, are in concurrence with the established criterion for predicting slip transmission (Lee et al., 1989).

The experimental estimates of $|b_r|$ that we established for each GB are similar to the transmission case shown in Fig. 11. As indicated earlier, several values of $|b_r|$ were calculated if multiple slip systems were activated in the mantle regions. Fig. 12(a) shows a histogram of the minimum $|b_r|$ for each of the transmitting GBs in the region of interest (~ 1000 GBs). Three distinct peaks in the number of GBs having similar $|b_r|$ are observed in Fig. 12(a). Most of these boundaries were characterized as $\Sigma 3$ type GBs, i.e., twins. The first peak is at $|b_r| = 0$. This magnitude of the residual Burgers vector is associated with cross slip leaving no residual in the GB plane (Hirth and Lothe, 1992), as shown schematically in Fig. 12(b). The second peak is at $|b_r| = |(a/6) < 211 >| = a/\sqrt{6}$; this type of reaction leaves a partial dislocation step at the GB as shown in Fig. 12(c). The third peak is at $|b_r| = |(a/2) < 101 >| = a/\sqrt{2}$, which leaves a full dislocation step at the GB as shown in Fig. 12(d). Examples of these three different cases, from our experimental results plotted in Fig. 12(a) are shown in Eqs. (13)–(15) below:

$$\frac{a}{2}[01\bar{1}]_1 \rightarrow \frac{a}{2}[\bar{1}\bar{1}0]_2 + b_r \Rightarrow b_r = 0 \Rightarrow |b_r| = 0 \quad (13)$$

$$\frac{a}{2}[101]_1 \rightarrow \frac{a}{2}[\bar{1}01]_2 + b_r \Rightarrow b_r = \frac{a}{6}[\bar{1}22]_1 \Rightarrow |b_r| = a/\sqrt{6} \quad (14)$$

$$\frac{a}{2}[110]_1 \rightarrow \frac{a}{2}[011]_2 + b_r \Rightarrow b_r = \frac{a}{2}[10\bar{1}]_1 \Rightarrow |b_r| = a/\sqrt{2}. \quad (15)$$

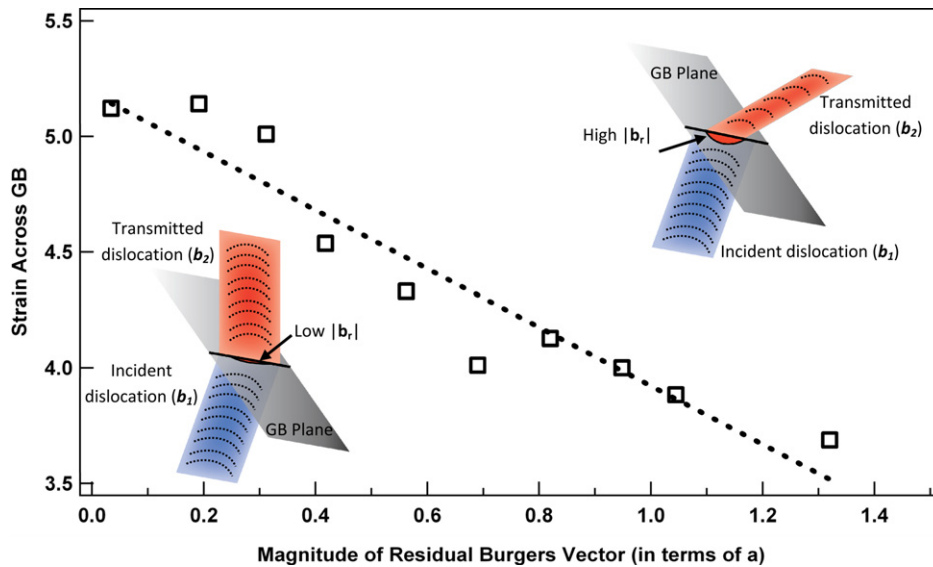


Fig. 13. Strain across grain boundaries versus residual Burgers vector. The strain across GBs is calculated by adding the average strains in both mantles across the boundary. Boundaries that show higher strains across the GB exhibit lower residual Burgers vectors. This can be related to the GB resistance to slip transmission.

To investigate the relation between $|b_r|$ and the accumulation of strain due to slip transmission, we used the experimentally determined estimates of $|b_r|$ and the strain measurements across GBs (mantle regions). First, we calculated the strain across each transmitting mantle in the region of interest, and then binned the GBs based on the minimum estimate of $|b_r|$ and finally calculated the average strain across the GBs for each bin. Fig. 13 shows a plot of strain across GBs versus $|b_r|$. Higher strains were measured across those GBs that have low $|b_r|$ indicating a lower GB resistance to slip transmission.

4. Molecular dynamics simulations

By the use of atomistic simulations, GBs are reconstructed from distinct orientations of crystal lattices (*i.e.*, $\Sigma 7$ GB – 38.2° twist about $[1\ 1\ 1]$ and $\Sigma 9$ GB – 38.9° tilt about $[1\ 1\ 0]$), which allows for direct calculation of the GB resistance to plastic deformation. The simulations consisted of Ni atoms using the Foiles-Hoyt Embedded Atom Method (EAM) potential (Foiles and Hoyt, 2006). This EAM potential was chosen to match the intrinsic, $\gamma_{SF}=127$ mJ/m², and unstable, $\gamma_{US}=255$ mJ/m², stacking fault energies of the material, which compare well with experimental values of 125–128 mJ/m² and *ab initio* calculations of 273 mJ/m² for the γ_{SF} and γ_{US} energies, respectively (Siegel, 2005). It is critical to obtain reasonable values of the unstable stacking fault energy as this parameter has been tied to the mechanics and nucleation of dislocations (Rice, 1992). We model the GB for this Ni-based superalloy as pure Ni. This is indeed a simplification, although a necessary one, given the difficulties in obtaining suitable cross pair-potentials between atoms.

Molecular Dynamics (MD) simulations are employed in the form of a Sandia National Laboratories code called LAMMPS (Plimpton, 1995, 2007). A single GB is constructed in each simulation, which is oriented horizontally across the simulation box. Periodic boundary conditions are enforced to allow for calculations of bulk material properties; hence the simulations are *not* restricted in length scale to nanocrystalline material. The simulation box is deformed using an NPT ensemble, where the number of atoms in the simulation box, N , the pressure in the three directions (stress free boundaries), P , and the system temperature, T (10 K), are held constant throughout the simulation. Uniaxial tension is applied perpendicular to the GB via a strain controlled test with a strain-rate of 10^{10} s⁻¹. This high strain-rate is indicative of MD simulations, although the results were verified with smaller strain-rates to ensure the same dislocation mechanics.

A void is introduced into the system to facilitate dislocation nucleation leading to slip-GB interaction, as shown in a schematic and atomistic snapshot view in Fig. 14(a) and (b), respectively. To grasp the role of the GBs on the energetics of each system, the potential energy of each atom was measured during the simulation. A control volume was placed at the intersection of the dislocation and GB along the atoms which play a role in the interaction (selected via the centrosymmetry parameter (CSP) (Kelchner et al., 1998); hence it is not a simple cubic box. Extreme care was taken to select the position of only the relevant defect atoms (as indicated by the CSP). By subtracting the energy of the atoms in the initial relaxed position from the total calculated energy (upon loading) and normalizing by the control volume, we arrive at the interaction energy. In order to verify these MD calculations of the energy barrier, a system was constructed without a GB to mimic slip in an fcc lattice. The result of our MD control volume method was in concurrence with the generalized stacking

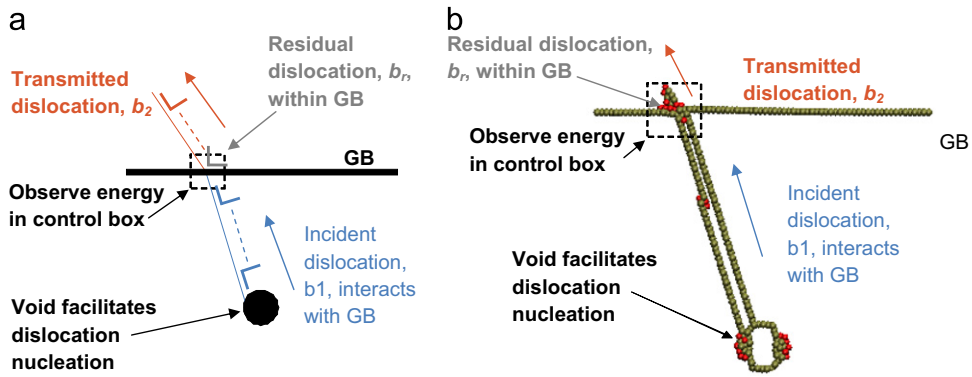


Fig. 14. (a) Schematic of control volume placed around the interaction region between the incident dislocation and the GB. This control volume is used to observe the energy during slip transmission. A void is used to nucleate a dislocation that eventually interacts with the GB and transmits to the other grain across the interface. (b) Atomistic snapshot view showing the slip-GB interaction similar to (a).

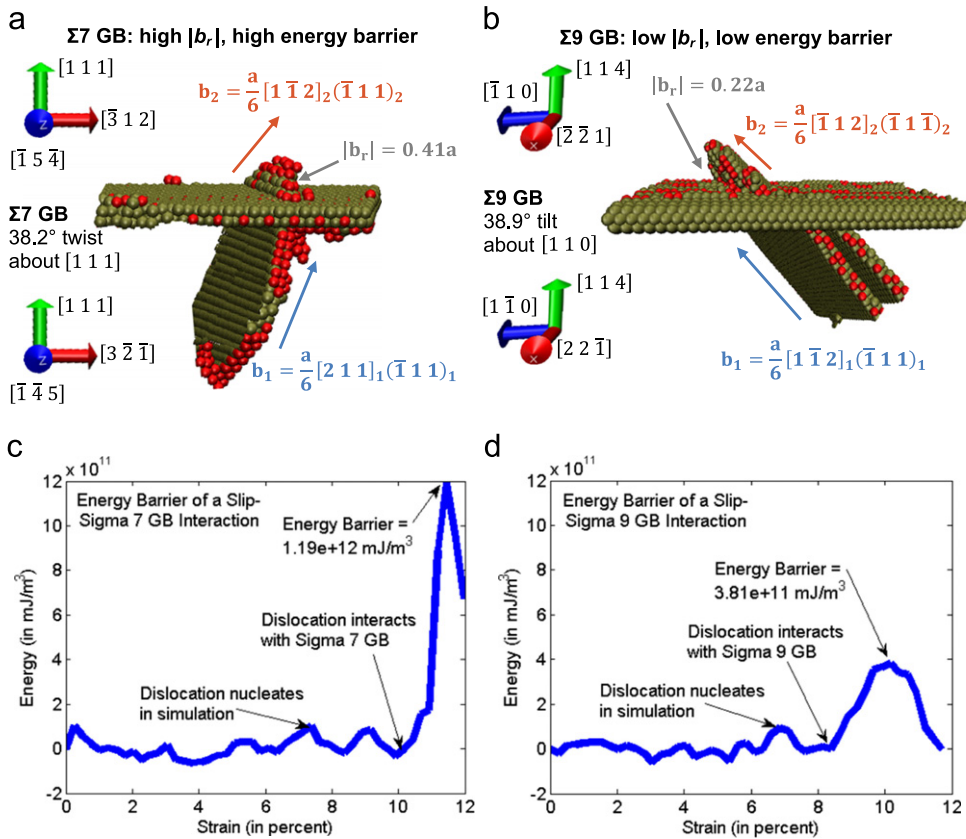


Fig. 15. (a) Dislocation transmission through a $\Sigma 7$ GB. (b) Dislocation transmission through a $\Sigma 9$ GB. Notice that the interaction with the $\Sigma 7$ GB leaves a higher $|b_r|$ compared to the $\Sigma 9$ GB ($0.41a > 0.22a$). The corresponding energy barriers shown in (c) and (d) show a higher energy barrier for slip transmission in the $\Sigma 7$ case (higher $|b_r|$) compared to the $\Sigma 9$ case (lower $|b_r|$), respectively.

fault energy and produced a modest 6% difference (Sangid et al., 2011), thus validating this procedure. Details concerning the methodology of these MD simulations can be found in Sangid et al. (2011).

This procedure was repeated for the CSL $\Sigma 7$ and $\Sigma 9$ GBs, as the slip-GB interaction and resulting dislocation reactions are shown in Fig. 15(a) and (b), respectively, using Visual Molecular Dynamics (Humphrey et al., 1996), an atomistic configuration viewer program. The CSP (Kelchner et al., 1998) is utilized to locate and color the defects within the material based on its position with respect to its nearest neighbors (red indicates a partial dislocation, while the golden color denotes a stacking fault). For clarity of presentation, defect-free atoms that do not participate in the interaction are deleted from the MD simulation snapshots. As expected, the incident dislocation is on a closed pack (1 1 1) plane, in the form of a leading partial

dislocation and in the shape of a loop containing mixed edge and screw components. After interaction with the GB, a partial dislocation is transmitted into the adjacent grain on a glissile plane. Given the dislocation reactions, the residual Burgers vector of the slip transmission process is calculated according to Eq. (9). The residual Burgers vector is $a/6[1\bar{1}2]$ in the case of slip transmission through a $\Sigma 7$ GB and $2a/27[\bar{2}\bar{2}1]$ for the $\Sigma 9$ GB. Therefore the magnitude of the residual Burgers vector is larger in the $\Sigma 7$ GB, $0.41a$, compared with the $\Sigma 9$ GB, $0.22a$, where a is the lattice constant of the material.

The resulting energy barriers for slip to penetrate the $\Sigma 7$ and $\Sigma 9$ GBs are shown in Fig. 15(c) and (d), respectively. The elastic strain energy of the system is removed from the energy calculations. The local fluctuations in energy due to temperature induced vibrations are small compared to the value of the energy barrier. Additionally, a local drop in energy is seen as the system nucleates a dislocation from the void. The energy of the system dramatically rises when the dislocation impinges upon the GB. The dislocation is temporarily impeded as the local energy builds at the site of slip-GB interaction. Once the dislocation traverses the GB, the energy of the system reduces as can be seen in the energy barrier profiles in Fig. 15(c) and (d). It can be seen that the $\Sigma 7$ GB provides a greater energy barrier to slip than the $\Sigma 9$ GB. In the cases shown, slip in the form of a leading partial dislocation interacts with a $\Sigma 7$ or $\Sigma 9$ GB, thus providing a consistent means for comparison. For the $\Sigma 9$ case, once the first partial has transmitted into the adjacent grain, a second partial travels towards the GB but we only consider the interaction of the first leading partial. Thus, the rise in energy associated with the slip – $\Sigma 9$ GB interaction in Fig. 15(b) is only based on the first dislocation interaction with the GB. The second leading partial is sufficiently far from the GB during slip transmission of the first partial, and does not affect the calculated barrier.

5. Discussion

The experimental and analysis procedure adopted in this study provides point-wise comparisons between strain fields (from DIC) and microstructure (from EBSD). The significance of this approach is that it enables quantitative analysis of local deformation in the vicinity of each GB within a polycrystalline aggregate. For each GB, we have identified the GB type (Σ value), crystallographic orientation, plastic strains, and local slip system activity in mantle regions across the interface. These experimental results were used to study slip transmission across GBs and how it relates to local strain heterogeneities in the plastic response. Although more details can be attained from higher resolution techniques, e.g., TEM, the limitations associated with small viewing areas makes considering a large number of grain boundaries, at comparatively lower resolutions, valuable for an improved understanding of the deformation response in the polycrystalline aggregate.

The full field DIC measurements show a high level of heterogeneity in the plastic response. The buildup of strains in some cases and the shielding in others was associated with deformation in mantle regions. In contrast, less scatter around the nominal residual strain was generally observed in grain interiors, i.e., cores. As the focus in this study is on deformation in the vicinity of grain boundaries, a distinction between core and mantle regions for each grain was made based on the experimental results. This kind of discretization of the measured strain fields was made possible through the utilization of high resolution DIC and EBSD. The strain contour plots (Fig. 3) and the strain histograms (Fig. 5) of mantle regions show a wide distribution of strain magnitudes in the vicinity of grain boundaries indicating that, at least at the applied strain levels employed here, not all mantles are in an advanced stage of hardening as we usually expect. Similar results from experiments (Tschopp et al., 2009) and simulations (Rollett et al., 2009) have been reported in the literature. Based on our experimental results we proposed a classification of each mantle as one of two types, high strain mantle or low strain mantle. We further associated these two types of mantles with shielding or slip transmission across GBs. In the case of shielding, the GBs have mantles with small and large strain combinations (Shielding mantles in Fig. 5); and in the case of transmission, both mantles exhibit high strains (Transmitting mantles in Fig. 5). This demarcation of mantles based on strain magnitudes allows a better characterization of the local plastic deformation and how it relates to the microstructure of the material. For example, as we show in this paper, some of the variations in plastic strain accumulation across GBs are attributed to different magnitudes of \mathbf{b}_r due to slip transmission.

In the current work, we have considered an entire aggregate and determined the residual Burgers vector and strain magnitudes across every GB due to slip transmission. The residual Burgers vector, \mathbf{b}_r , was calculated using the slip directions of the incoming and outgoing active slip systems across each GB (Eq. (10)) and the strain magnitudes across GBs were computed by adding the average ϵ_{eff}^p in both mantles across each interface. Since a large number of GBs were investigated, we were able to establish the relation between $|\mathbf{b}_r|$ and the magnitudes of strain across GBs (Fig. 13). The higher strains across certain boundaries, at low $|\mathbf{b}_r|$, are attributed to lower GB resistance against slip transmission, while lower strains across GBs, at high $|\mathbf{b}_r|$, are attributed to higher GB resistance against slip transmission. This result confirms the importance of the residual Burgers vector in slip transmission (Lim, 1984; Lim and Raj, 1985; Lee et al., 1989) and also indicates that it is essential for describing the local strain magnitudes in the vicinity of GBs for a polycrystalline aggregate.

An additional level of understanding of the role of $|\mathbf{b}_r|$ in slip transmission was obtained from Molecular Dynamics (MD) simulations by calculating the energy barriers against slip transmission. As our aim was to further elucidate the relation between $|\mathbf{b}_r|$ and GB resistance to slip transmission, two simulation cases that result in different magnitudes of \mathbf{b}_r were considered here (shown in Fig. 15(a) and (b)). In the first case, we observe transmission through a $\Sigma 7$ GB. This interaction left a higher residual Burgers vector compared to the other simulated case, where transmission through a $\Sigma 9$ GB was considered ($0.41a > 0.22a$, where a is the lattice spacing). The corresponding energy barriers presented in Fig. 15(c) and (d) show a higher energy barrier for the $\Sigma 7$ case (higher $|\mathbf{b}_r|$) compared to the $\Sigma 9$ case (lower $|\mathbf{b}_r|$). This difference in energy barriers, analogous to the GB resistance to slip transmission, leads to varying degrees of strain magnitudes across the GBs as shown in Fig. 13, i.e., higher slip induced

strains across the GBs with lower resistance to slip transmission. This utilization of MD for energy barriers calculations is valuable since we can more accurately interpret the role of each GB in impeding slip deformation by understanding the physics of the material. We emphasize that the use of MD in conjunction with EBSD and DIC provides insights that cannot be gleaned by consideration of only one of these methods.

It should be pointed out that slip transmission depends not only on the magnitude of \mathbf{b}_r but also on other parameters such as the type of the boundary, loading conditions, *i.e.*, resolved shear stress (RSS), and the geometric condition, θ , (Fig. 10). Lee et al. (1989) have indicated that there is a competition between \mathbf{b}_r and the RSS to determine the final outcome of the slip transmission process. The systems that produce the absolute minimum residual might not be active due to lower RSS compared to other systems. Also, an activated system with the maximum RSS may cease operation if it generates residual dislocations with large magnitudes. Therefore, within a polycrystalline aggregate, where each grain is under a different state of stress, consideration of both of these factors is required for a better description of the GB resistance to slip transmission.

We infer three different types of reactions involving twin boundaries ($\Sigma 3$ GBs) as shown in Fig. 12. The same types of reactions were experimentally observed through TEM and reported in the literature for selected transmission cases (fcc materials), *e.g.*, $|\mathbf{b}_r|=0$, *i.e.*, cross slip (Lee et al., 1989) and $|\mathbf{b}_r|=a/\sqrt{6}$, *i.e.*, leaving partial dislocation step in the GB plane (Lee et al., 1990). Also, some of these reactions have been reported and discussed in much more detail in studies using MD simulations (Dewald and Curtin, 2011). The current study reports similar magnitudes of \mathbf{b}_r by investigating a large number of grain boundaries in a polycrystalline aggregate. This approach provides further quantitative insight of the relative importance of each of the observed reactions, involving $\Sigma 3$ GBs, in polycrystalline deformation. For example, we observe that the number of transmitting $\Sigma 3$ GBs with $|\mathbf{b}_r|=0$ is considerably larger than the number of $\Sigma 3$ GBs with $|\mathbf{b}_r|=a/\sqrt{6}$ or $|\mathbf{b}_r|=a/\sqrt{2}$ (Fig. 12). This in turn results in higher strain magnitudes across these interfaces, with $|\mathbf{b}_r|=0$, compared to other GBs.

The experimental results presented in this paper highlight the importance of the magnitude of the residual Burgers vector due to slip transmission on the local plastic strains in the vicinity of grain boundaries. It should be pointed out that, although some of the heterogeneities in the local plastic strains are attributed to slip transmission, slip transfer is not the only contributing mechanism to the development of such heterogeneities, *e.g.*, slip nucleation and elastic anisotropy have a contribution which we do not account for in the current study. Therefore, for a deeper perspective of the reasons why strain accumulation occurs at certain boundaries and not at others, and to discern between slip transmission and pure nucleation that might also take place at the GBs, further analysis of the other contributing mechanisms would be required. *In situ* experiments can be advantageous in that regard as deformation can be monitored in real time compared to *ex situ* experiments (*i.e.*, after deformation) as performed in this study. However, there are many challenges related to the experimental setup and procedure which have to be overcome before such *in situ* experiments are possible (Carroll et al., 2010). In addition, *ex situ* experiments afford a much higher resolution of DIC measurements than *in situ* ones.

Another limitation that is worth pointing out is the fact that all the analyses have been performed on the surface of the material. No insight into subsurface effects is possible through the utilization of the DIC and EBSD techniques as employed in this study. This particular issue can be addressed with a combination of high energy X-ray diffraction for three dimensional orientation mapping (Lienert et al., 2011) and crystal plasticity simulations (Rollett et al., 2010). Internal strain measurements could be performed using Digital Volume Correlation – a 3D extension of DIC – but this is a method still under development (Gates et al., 2011). Therefore, high resolution DIC measurements, as performed in this study, are only possible at the surface. Careful experimental and simulation work which utilizes all of the previously mentioned techniques would help further explorations of subsurface effects and how they influence, for example, slip transmission across GBs.

Despite the previously mentioned limitations, which might affect the results obtained at individual GBs, we believe that the impact on the general observations made in the current work would be minimum as the average response of a large number of GBs was considered to make the final conclusions presented in this paper.

6. Conclusions

High resolution DIC and EBSD were used to study the uniaxial plastic deformation response of a polycrystalline sample in relation to the underlying microstructure. The aim of the work was to develop a deeper perspective of strain accumulation in the vicinity of grain boundaries within a polycrystalline aggregate. The conclusions of this study are summarized as follows:

1. We present an experimental and analysis procedure, that provides point-wise comparisons between strain fields (from DIC) and microstructure (from EBSD). The significance of this approach is that it enables quantitative analysis of local deformation in the vicinity of every grain boundary within a polycrystalline aggregate. These experimental tools were utilized to provide further insight into the role of the residual Burgers vector in slip transmission and plastic strain accumulation in the vicinity of GBs. This correlation between plastic strain magnitudes across GBs and the residual Burgers vector has not been investigated before. A better quantitative understanding of the local plastic strain magnitudes is of significant importance since the development of such deformation heterogeneities is a precursor to crack initiation.

2. For an entire aggregate, we determined the residual Burgers vector and strain magnitudes across every GB due to slip transmission. Since a large number of GBs was investigated, we were able to establish an inverse relation between $|\mathbf{b}_r|$ and the magnitudes of strain across GBs. To the best of our knowledge, no similar results have been presented in the literature where such a large number of GBs was considered with sufficient details to derive general conclusion concerning the impact of slip transmission on the development of local deformation heterogeneity.
3. The MD simulations revealed a higher energy barrier to slip transmission at high $|\mathbf{b}_r|$. These energy barriers, analogous to the GB resistance to slip transmission, have an influence on the strain magnitudes across GBs.
4. The higher strains across certain boundaries, at low $|\mathbf{b}_r|$, were associated with lower GB resistance against slip transmission while lower strains across GBs, at high $|\mathbf{b}_r|$, were attributed to higher resistance against slip transmission.
5. The reactions we inferred for slip transmission across $\Sigma 3$ GBs revealed a larger number of boundaries with $|\mathbf{b}_r|=0$, *i.e.*, cross slip, compared to other types of reaction resulting in higher magnitudes of the residual Burgers vector. This in turn results in higher strain magnitudes across these interfaces, with $|\mathbf{b}_r|=0$, compared to other GBs.
6. We made a distinction between core and mantle regions for each grain through the utilization of high resolution DIC and EBSD. We also proposed a classification of each mantle as a high or low strain mantle and associated these two types of mantles with shielding or slip transmission across GBs. This demarcation of mantles based on strain magnitudes allows a better characterization of the local plastic deformation and how it relates to the microstructure of the material.

Acknowledgments

This work was supported by the Midwest Structural Sciences Center (MSSC), which is supported by the Air Vehicles Directorate of the U.S. Air Force Research Laboratory under contract number FA8650-06-2-3620. The work is also partially supported by NSF grants CMMI-09-26813 and partly by DMR-08-03270. The authors thank Prof. Armand J. Beaudoin for enlightening discussions. EBSD results were obtained with the assistance of Dr. Jim Mabon at the Frederick Seitz Materials Research Laboratory Central Facilities, University of Illinois, which are partially supported by the U.S. Department of Energy under grants DE-FG02-07ER46453 and DE-FG02-07ER46471.

Appendix

This appendix provides details of the coordinate transformation between crystal and sample frames. We also report the procedure followed to calculate the Schmid factors, shown for example in Table 1, from EBSD crystal orientation measurement (*i.e.*, Euler angles).

1. Using the Euler angles $(\varphi_1, \Phi, \varphi_2)$, the rotation matrix \mathbf{g} is determined using the following equation (Bunge definition).

$$\mathbf{g} = \begin{bmatrix} \cos \varphi_1 \cos \varphi_2 - \sin \varphi_1 \sin \varphi_2 \cos \Phi & \sin \varphi_1 \cos \varphi_2 + \cos \varphi_1 \sin \varphi_2 \cos \Phi & \sin \varphi_2 \sin \Phi \\ -\cos \varphi_1 \sin \varphi_2 - \sin \varphi_1 \cos \varphi_2 \cos \Phi & -\sin \varphi_1 \sin \varphi_2 + \cos \varphi_1 \cos \varphi_2 \cos \Phi & \cos \varphi_2 \sin \Phi \\ \sin \varphi_1 \sin \Phi & -\cos \varphi_2 \sin \Phi & \cos \Phi \end{bmatrix} \quad (\text{A1})$$

2. To transform from sample frame to crystal frame, the following equations are used

$$\mathbf{C}_{\text{crystal}} = \mathbf{g} \mathbf{C}_{\text{sample}} \quad (\text{where } \mathbf{C} \text{ is a vector}) \quad (\text{A2})$$

$$\mathbf{A}_{\text{crystal}} = \mathbf{g} \mathbf{A}_{\text{sample}} \mathbf{g}^{-1} \quad (\text{where } \mathbf{A} \text{ is a second order tensor, e.g., strain tensor } \boldsymbol{\varepsilon}_{ij}) \quad (\text{A3})$$

3. The Schmid factor for a particular slip system α , that is defined by slip plane normal \mathbf{n}^α and slip direction \mathbf{l}^α , can be found using the following equation:

$$\text{Schmid Factor}^\alpha = |(\mathbf{L}_{\text{crystal}} \cdot \mathbf{n}^\alpha)(\mathbf{L}_{\text{crystal}} \cdot \mathbf{l}^\alpha)| \quad (\text{A4})$$

where $\mathbf{L}_{\text{crystal}}$ is the loading direction written in crystal frame (found using Eq. (A2)). All vectors in Eq. (A4) are unit vectors. \mathbf{n}^α and \mathbf{l}^α are known for fcc crystals (listed in Table 1).

4. From DIC we establish the strain tensor in sample frame ($\boldsymbol{\varepsilon}_{\text{sample}}$). To write the strain tensor in crystal frame, Eq. (A3) is used.

$$\boldsymbol{\varepsilon}_{\text{crystal}} = \mathbf{g} \boldsymbol{\varepsilon}_{\text{sample}} \mathbf{g}^{-1} \quad (\text{A5})$$

References

- Bartali, A.E., Aubin, V., Degallaix, S., 2009. Surface observation and measurement techniques to study the fatigue damage micromechanisms in a duplex stainless steel. *Int. J. Fatigue* 31, 2049.

- Bieler, T.R., Eisenlohr, P., Roters, F., Kumar, D., Mason, D.E., Crimp, M.A., Raabe, D., 2009. The role of heterogeneous deformation on damage nucleation at grain boundaries in single phase metals. *Int. J. Plast.* 25, 1655.
- Carroll, J., Abuzaid, W., Lambros, J., Sehitoglu, H., 2010. An experimental methodology to relate local strain to microstructural texture. *Rev. Sci. Instrum.* 81, 083703.
- Dewald, M., Curtin, W.A., 2011. Multiscale modeling of dislocation/grain-boundary interactions: III. 60° dislocations impinging on $\Sigma 3$, $\Sigma 9$ and $\Sigma 11$ tilt boundaries in Al. *Modell. Simul. Mater. Sci. Eng.*, 19.
- Dewald, M.P., Curtin, W.A., 2007a. Multiscale modelling of dislocation/grain-boundary interactions: I. Edge dislocations impinging on $\Sigma 11$ (1 1 3) tilt boundary in Al. *Modell. Simul. Mater. Sci. Eng.* 15, S193.
- Dewald, M.P., Curtin, W.A., 2007b. Multiscale modelling of dislocation/grain boundary interactionsII. Screw dislocations impinging on tilt boundaries in Al. *Philos. Mag.* 87, 4615.
- Efstathiou, C., Sehitoglu, H., Lambros, J., 2010. Multiscale strain measurements of plastically deforming polycrystalline titanium: role of deformation heterogeneities. *Int. J. Plast.* 26, 93.
- Engler, O., Randle, V., 2010. *Introduction to Texture Analysis*, 2nd edn CRC Press.
- Eshelby, J.D., Frank, F.C., Nabarro, F.R.N., 1951. The equilibrium of linear arrays of dislocations. *Philos. Mag.* 42, 351–364.
- Ezaz, T., Sangid, M.D., Sehitoglu, H., 2010. Energy barriers associated with slip-twin interactions. *Philos. Mag.* 91, 1464–1488.
- Foiles, S.M., Hoyt, J.J., 2006. Computation of grain boundary stiffness and mobility from boundary fluctuations. *Acta Mater.* 54, 3351.
- Gates, M., Lambros, J., Heath, M., 2011. Towards high performance digital volume correlation. *Exp. Mech.* 51, 491.
- Hall, E.O., 1951. The deformation and aging of mild steel:III. Discussion of results. *Proc. Phys. Soc. London* 64, 747–753.
- Hirth, J., Lothe, J., 1992. *Theory of Dislocations*, 2nd edn. Krieger Publishing Company.
- Huang, J., Pelloux, R., 1980. Low cycle fatigue crack propagation in hastelloy- X at 25 and 760 °C. *Metall. Mater. Trans. A* 11, 899.
- Humphrey, W., Dalke, A., Schulten, K., 1996. VMD: visual molecular dynamics. *J. Mol. Graphics* 14, 33.
- Hutchinson, J.W., 1976. Bounds and Self-consistent estimates for creep of polycrystalline materials. *Proceedings of the Royal Society of London Series A. NATO ASI Ser.*, Ser. C 348, 101.
- Jin, Z.H., Gumbsch, P., Albe, K., Ma, E., Lu, K., Gleiter, H., Hahn, H., 2008. Interactions between non-screw lattice dislocations and coherent twin boundaries in face-centered cubic metals. *Acta Mater.* 56, 1126.
- Kelchner, C.L., Plimpton, S.J., Hamilton, J.C., 1998. Dislocation nucleation and defect structure during surface indentation. *Phys. Rev. B* 58, 11085.
- Kim, W.-G., Yin, S.-N., Kim, Y.-W., Chang, J.-H., 2008. Creep characterization of a Ni-based Hastelloy-X alloy by using theta projection method. *Eng. Fract. Mech.* 75, 4985.
- Kocks, U.F., Chandra, H., 1982. Slip geometry in partially constrained deformation. *Acta Metall.* 30, 695.
- Lee, T.C., Robertson, I.M., Birnbaum, H.K., 1989. Prediction of slip transfer mechanisms across grain boundaries. *Scr. Metall.* 23, 799.
- Lee, T.C., Robertson, I.M., Birnbaum, H.K., 1990. An *In Situ* transmission electron microscope deformation study of the slip transfer mechanisms in metals. *Metall. Trans. A* 21, 2437.
- Lienert, U., Li, S., Hefferan, C., Lind, J., Suter, R., Bernier, J., Barton, N., Brandes, M., Mills, M., Miller, M., Jakobsen, B., Pantleon, W., 2011. High-energy diffraction microscopy at the advanced photon source. *JOM Journal of the Minerals, Metals and Materials Society* 63, 70.
- Lim, L.C., 1984. Slip-twin interactions in nickel at 573 K at large strains. *Scr. Metall.* 18, 1139.
- Lim, L.C., Raj, R., 1985. Continuity of slip screw and mixed crystal dislocations across bicrystals of nickel at 573 K. *Acta Metallurgica* 33, 1577.
- Livingston, J.D., Chalmers, B., 1957. Multiple slip in bicrystal deformation. *Acta Metall.* 5, 322.
- Meyers, M.A., Ashworth, E., 1982. Model for the effect of grain size on the yield stress of metals. *Philos. Mag. A*: 46, 737.
- Miner, R., Castelli, M., 1992. Hardening mechanisms in a dynamic strain aging alloy, HASTELLOY X, during isothermal and thermomechanical cyclic deformation. *Metall. Mater. Trans. A* 23, 551.
- Petch, N.J., 1953. The cleavage strength of polycrystals. *J. Iron. Steel Inst.* 174, 25–28.
- Plimpton, S., 1995. Fast parallel algorithms for short-range molecular dynamics. *J. Comput. Phys.* 117, 1–19.
- Plimpton, S., 2007. Large-scale Atomic/Molecular Massively Parallel Simulator. Sandia National Laboratories.
- Rice, J.R., 1992. Dislocation nucleation from a crack tip: an analysis based on the Peierls concept. *J. Mech. Phys. Solids* 40, 239.
- Rollett, A.D., Lebensohn, R.A., Groeber, M., Choi, Y., Li, J., Rohrer, G.S., 2009. Stress hot spots in viscoplastic deformation of polycrystals. *Modell. Simul. Mater. Sci. Eng.*, 18.
- Rollett, A.D., Lebensohn, R.A., Groeber, M., Choi, Y., Li, J., Rohrer, G.S., 2010. Stress hot spots in viscoplastic deformation of polycrystals. *Modell. Simul. Mater. Sci. Eng.*, 18.
- Roters, F., Eisenlohr, P., Hantcherli, L., Tjahjanto, D.D., Bieler, T.R., Raabe, D., 2010. Overview of constitutive laws, kinematics, homogenization and multiscale methods in crystal plasticity finite-element modeling: theory, experiments, applications. *Acta Mater.* 58, 1152.
- Rowley, M.A., Thornton, E.A., 1996. Constitutive modeling of the visco-plastic response of Hastelloy-X and aluminum alloy 8009. *J. Eng. Mater. Technol.* 118, 19.
- Sangid, M.D., Ezaz, T., Sehitoglu, H., Robertson, I.M., 2011. Energy of slip transmission and nucleation at grain boundaries. *Acta Mater.* 59, 283.
- Shen, Z., Wagoner, R.H., Clark, W.A.T., 1986. Dislocation pile-up and grain boundary interactions in 304 stainless steel. *Scr. Metall.* 20, 921.
- Siegel, D.J., 2005. Generalized stacking fault energies, ductilities, and twinnabilities of Ni and selected Ni alloys. *Appl. Phys. Lett.* 87, 121901.
- Sutton, A.P., Balluffi, R.W., 2006. *Interfaces in Crystalline Materials*. Oxford Classical Texts, Oxford.
- Sutton, M.A., Wolters, W.J., Peters, W.H., Ranson, W.F., McNeill, S.R., 1983. Determination of displacements using an improved digital correlation method. *Image Vision Comput.* 1, 133.
- Tatschl, A., Kolednik, O., 2003. On the experimental characterization of crystal plasticity in polycrystals. *Mater. Sci. Eng.*, A 356, 447.
- Taylor, G.I., 1938. Plastic strain in metals. *J. Inst. Met.* 62, 307–325.
- Tschopp, M.A., Bartha, B.B., Porter, W.J., Murray, P.T., Fairchild, S.B., 2009. Microstructure-dependent local strain behavior in polycrystals through *In-Situ* Scanning Electron Microscope Tensile Experiments. *Metall. Mater. Trans. A* 40, 2363.
- Zhang, N., Tong, W., 2004. An experimental study on grain deformation and interactions in an Al-0.5%Mg multicrystal. *Int. J. Plast.* 20, 523.
- Zhao, Z., Ramesh, M., Raabe, D., Cuitiño, A.M., Radovitzky, R., 2008. Investigation of three-dimensional aspects of grain-scale plastic surface deformation of an aluminum oligocrystal. *Int. J. Plast.* 24, 2278.